Lagrangian chaos in steady three-dimensional lid-driven cavity flow

Francesco Romanò,[1,a)] Tuğçe Türkbay,[2] and Hendrik C. Kuhlmann[3]

AFFILIATIONS

[1]Univ. Lille, CNRS, ONERA, Arts et Métiers, Centrale Lille, FRE 2017-LMFL—Laboratoire de Mécanique des Fluides de Lille—Kampé de Fériet, F-59000 Lille, France
[2]Department of Automotive Engineering, University of Afyon Kocatepe, Ahmet Necdet Sezer Kampüsü Gazlıgöl Yolu, 03200 Afyonkarahisar, Turkey
[3]Institute of Fluid Mechanics and Heat Transfer, TU Wien, Getreidemarkt 9, 1060 Vienna, Austria

[a)]**Author to whom correspondence should be addressed:** francesco.romano@ensam.eu

ABSTRACT

Steady three-dimensional flows in lid-driven cavities are investigated numerically using a high-order spectral-element solver for the incompressible Navier–Stokes equations. The focus is placed on critical points in the flow field, critical limit cycles, their heteroclinic connections, and on the existence, shape, and dependence on the Reynolds number of Kolmogorov–Arnold–Moser (KAM) tori. In finite-length cuboidal cavities at small Reynolds numbers, a thin layer of chaotic streamlines covers all walls. As the Reynolds number is increased, the chaotic layer widens and the complementary KAM tori shrink, eventually undergoing resonances, until they vanish. Accurate data for the location of closed streamlines and of KAM tori are provided, both of which reach very close to the moving lid. For steady periodic Taylor–Görtler vortices in spanwise infinitely extended cavities with a square cross section, chaotic streamlines occupy a large part of the flow domain immediately after the onset of Taylor–Görtler vortices. As the Reynolds number increases, the remaining KAM tori vanish from the Taylor–Görtler vortices, while KAM tori grow in the central region further away from the solid walls.

The streamline topology of the steady flow in three-dimensional lid-driven cavities is thoroughly investigated. Regions of chaotic and regular streamlines are identified by accurate numerical simulations. The dependence of the Kolmogorov–Arnoldi–Moser (KAM) tori on the Reynolds number, geometric parameters, and the boundary conditions (finite length or periodic cavity) is elucidated. Geometrical indicators of the flow topology are introduced and determined in order to quantitatively characterize the regular (periodic and quasiperiodic) streamlines of the flow.

I. INTRODUCTION

Streamlines in incompressible closed flows are either chaotic or regular. Regular streamlines, i.e., closed or quasiperiodic streamlines, coexist with chaotic streamlines in the same flow (Aref, 1986) such that fluid elements from regular regions never enter chaotic regions and vice versa. Since the spreading of passive scalars is much more efficient in chaotic regions than in regular regions of the flow, the streamline topology is of key importance for mixing processes (Ottino, 1989). Furthermore, closed streamlines embedded in regular regions may serve as templates for coherent structures of advected finite-size particles (Romanò *et al.*, 2019).

Streamline topologies in closed systems have been investigated mainly for incompressible two-dimensional time-dependent flows for which a theoretical framework in terms of Hamiltonian dynamics is well established. In this analogy, the stream function of the two-dimensional flow is identified as the Hamiltonian of a corresponding dynamical system with one degree of freedom, and the Cartesian coordinates take the role of the generalized position and momentum. On the other hand, a canonical Hamiltonian theory for steady three-dimensional incompressible flows is not yet fully developed (Wiggins, 2010), even though important elements are available. For instance, the existence of invariant curves and tori in three-dimensional volume-preserving flows has been proven by Cheng and Sun (1989a; 1989b). Moreover, the KAM theorem (Arnol'd, 1978), which describes the response of nonresonant invariant tori to small perturbations of the system, has been

generalized to three-dimensional systems by Cheng and Sun (1990), Mezić and Wiggins (1994), and Broer *et al.* (2009). An important element of a full Hamiltonian description of three-dimensional volume-preserving flows was provided by Bajer (1994) who showed that a three-dimensional steady incompressible Navier–Stokes flow is locally equivalent to a Hamiltonian system with 1.5 degrees of freedom. In this local theory, the phase space is identical with the configuration space, while the velocity vector $\boldsymbol{u}(\boldsymbol{x})$ represents the flux in the phase space. This analogy, however, breaks down near stagnation points of the flow, which play an important role in the chaotic dynamics. This breakdown prevents an extension of the local Hamiltonian framework to a general three-dimensional theory.

Regardless of this difficulty, it is well known that regular and chaotic trajectories/streamlines can coexist in three-dimensional steady Navier–Stokes flows, and the local analogy with Hamiltonian systems implies that the regular motion arises in the form of Kolmogorov–Arnold–Moser tori or spheroids (Aref *et al.*, 2017). The importance and significance of this coexistence in steady laminar flows has been elaborated by Aref (1983; 1984), Aref and Balachandar (1986), and Aref (1990; 2002). The kinematic template of the flow is also important for chaotic mixing, i.e., the mixing of a fluid with itself, the mathematical foundations of which have been reviewed by Aref *et al.* (2017).

Due to the incomplete theoretical framework and the high numerical resolution required to reliably compute three-dimensional streamlines for the necessary long periods of time, only a few genuinely three-dimensional fluid systems have been thoroughly investigated in the literature. Examples are flows for which closed-form solutions or approximations of Navier–Stokes flows are available (Arter, 1983; Broomhead and Ryrie, 1988; Kroujiline and Stone, 1999; and Muldoon and Kuhlmann, 2013). Other investigations were concerned with streamline chaos in spatially three-dimensional Stokes flows and weakly inertial flows (Anderson *et al.*, 1999; Shankar, 1998; Cartwright *et al.*, 1996; and Pouransari *et al.*, 2010). Tackling steady nonlinear incompressible Navier–Stokes flows at moderate Reynolds numbers has become more feasible only recently (see, e.g., Fountain *et al.*, 2000; Ishii *et al.*, 2012; Mukin and Kuhlmann, 2013; Romanò and Kuhlmann, 2018; and Contreras *et al.*, 2019).

The incompressible flow of a Newtonian fluid in a lid-driven cavity is very well suited for fundamental investigations of the streamline topology of laminar vortices (Chien *et al.*, 1986; Leong and Ottino, 1989; and Franjione *et al.*, 1989). In the classical setup, a single lid moves tangentially to itself and parallel to the edge of a cuboid. Several variants of the system exist, depending on the number of moving walls, the directions in which they move (Povitsky, 2017), and on the velocity protocols. The lid-driven cavity problem has been introduced by Burggraf (1966). Since the investigations of Koseff (1984) it has become a paradigm for the study of closed vortex flows. While the problem is a popular numerical benchmark (Ghia *et al.*, 1982; Botella and Peyret, 1998; Albensoeder and Kuhlmann, 2005; Bruneau and Saad, 2006; and Romanò and Kuhlmann, 2017b), it has also been used to model a number of industrial applications, such as coating (Gaskell *et al.*, 1996), condensation drying (Alleborn *et al.*, 1999), and noise reduction (Crighton, 1991). Despite its simple geometry, the lid-driven cavity exhibits a rich variety of fluid dynamics phenomena, which are related to fundamental problems. One fundamental problem, the Taylor scraper problem (Taylor, 1960; 1962), is concerned with the local flow near the edge made by a moving and a stationary wall. Yet another example in a two-dimensional cavity flow is the infinite sequence of viscous eddies in the corner between two stationary walls, which has been discovered and investigated by Moffatt (1964). The corresponding extension to trihedral corners has been extensively studied in recent years (see, e.g., Gomilko *et al.*, 2003; Scott, 2013; and Davis and Smith, 2014). The lid-driven cavity has also been recently employed to test the extension of the Prandtl–Batchelor theorem (Prandtl, 1904; Batchelor, 1956) to quasiperiodic flows (Arbabi and Mezić, 2019). Finally, the two-dimensional steady flow in lid-driven cavities may not be unique (Albensoeder *et al.*, 2001a) and may become unstable due to centrifugal, elliptic, quadripolar, or other instability mechanisms (Ramanan and Homsy, 1994; Albensoeder *et al.*, 2001b; Auteri *et al.*, 2002; and Albensoeder and Kuhlmann, 2002; 2003). Reviews on lid-driven cavities have been given by Shankar and Deshpande (2000) and Kuhlmann and Romanò (2019). While Shankar and Deshpande (2000) treated flow structures and streamline patterns, also including other geometries such as cylindrical cavities, Kuhlmann and Romanò (2019) paid more attention to recent developments concerning three-dimensional flow instabilities and nonlinear supercritical dynamics.

Chaotic mixing of a laminar two-dimensional cavity flow was experimentally investigated by Chien *et al.* (1986). They considered a cavity in which the tangential motion of two facing lids was prescribed according to a certain time-dependent protocol such that $\mathrm{Re} = O(1)$. However, neither the conditions under which global chaos arises could be predicted nor could a good overall mixing be achieved. Mixing in time-dependent two-dimensional cavity flows was further elaborated by Leong and Ottino (1989). In rectangular cavity flows and other systems mixing was discussed by Ottino *et al.* (1988) emphasizing the horseshoe concept of Smale in which repeated folding and stretching leads to a chaotic dynamics. The book of Ottino (1989) gives a fundamental introduction to the field. The studies of periodically-driven two-dimensional cavities at small Reynolds numbers have been extended by Anderson *et al.* (2000) who included flow inertia by considering Reynolds numbers up to $\mathrm{Re} = \mathcal{O}(50)$. With flow inertia, the presence of KAM tori can enhance the global mixing inside the cavity. Recent investigations focused on Reynolds number protocols designed to optimize the mixing of the fluid and also of a particulate phase immersed in the fluid (Hwang *et al.*, 2005; Xu and Gilchrist, 2010; and Pai *et al.*, 2013). Owing to inertia and shear migration of the particles, the protocols for an optimum mixing of the fluid may differ significantly from those required for an efficient mixing of the particles.

Concerning the general streamline topology, Biemond *et al.* (2008) have shown that two-dimensional open flows with stagnation points on the boundary or separatrices, which represent transport barriers, become immediately chaotic as the flow is perturbed by the onset of time-dependence. Steady three-dimensional perturbations may follow the same route to chaos (Arter, 1983; Chernikov and Schmidt, 1992; and Romanò *et al.*, 2017). The first report on the Lagrangian flow structure in a steady rectangular lid-driven cavity flow is due to Ishii and Iwatsu (1989) who detected KAM tori by the use of Poincaré sections. Their results are also referred to by Shankar and Deshpande (2000). Thereafter, several parameter

variations were considered. Ishii and Adachi (2006) computed the flow topology with the emphasis on KAM tori as a function of the Reynolds number ranging from 100 to 850 in a cavity with a square cross section and a spanwise extent of 6.55 times the cavity height. In more recent numerical studies, Ishii and Adachi (2011) and Ishii *et al.* (2012) focused on resonance phenomena by which higher-order KAM tori are created upon an increase of the Reynolds number. The evolution of the streamline topology of the steady periodic cellular flow in a two-sided lid-driven cavity was considered by Romanò *et al.* (2017). As the two-dimensional basic flow bifurcates to the three-dimensional cellular flow, all streamlines become chaotic immediately. Only for higher Reynolds numbers, KAM tori appear, which vanish again at higher Reynolds numbers. It should be noted that the flow topology was also considered in cylindrical cavities, either driven by lid translation (Znaien *et al.*, 2012) or rotation (Fountain *et al.*, 2000).

The topology of a steady three-dimensional flow is not only important for mixing of fluids with itself, but also for the transport of suspended particles. While small density-matched particles far from boundaries perfectly follow the flow, they may accumulate in or near KAM tori either as inertial coherent structures due to particle inertia (Haller, 2015) or as finite-size Lagrangian coherent structures due to particle size (Hofmann and Kuhlmann, 2011). For the three-dimensional cellular flow in a two-sided lid-driven cavity, the existence of these latter structures has been demonstrated by Romanò *et al.* (2019). Since these finite-size coherent structures (FSCSs) depend on the KAM tori of the flow, their precise characterization is of crucial importance. Similar particulate structures have also been observed in related systems (Mukin and Kuhlmann, 2013; Romanò *et al.*, 2017; Romanò and Kuhlmann, 2017b, 2019; and Barmak *et al.*, 2019).

In the present work, we analyze the streamline structure in cavity flows driven by a single lid with a constant velocity. We build on the work of Ishii and Adachi (2006; 2011) and Ishii *et al.* (2012) to more precisely characterize the topology of the KAM tori in this system. A precise knowledge of regular vs chaotic regions of the flow helps understand the motion of nearly advected particles in cavities and should lead to an improved understanding of previous results such as those of Tsorng *et al.* (2006; 2008). Furthermore, we extend the analysis to periodic Taylor–Görtler vortices arising above the critical Reynolds number in a cavity with a square cross section, which is infinitely extended in a spanwise direction. The problem is formulated in Sec. II. Section III treats the numerical methods employed to compute the flow and its streamlines. Results for flows in finite-length cavities and for spanwise periodic flows are presented in Secs. IV and V, respectively. We close with a summary and discussion in Sec. VI.

II. PROBLEM FORMULATION

We consider the flow in a rectangular cuboid filled with an incompressible Newtonian fluid of the density ρ and the kinematic viscosity ν as shown in Fig. 1. The origin of a Cartesian coordinate system aligned with the edges of the cuboid is placed in one of the bottom corners. The geometry is defined by the depth D in the x-direction, the height H in the y-direction, and the length L in the z-direction. The flow is driven by the motion of the wall at $y = H$ in the positive x-direction, tangentially to itself and with a constant velocity U.

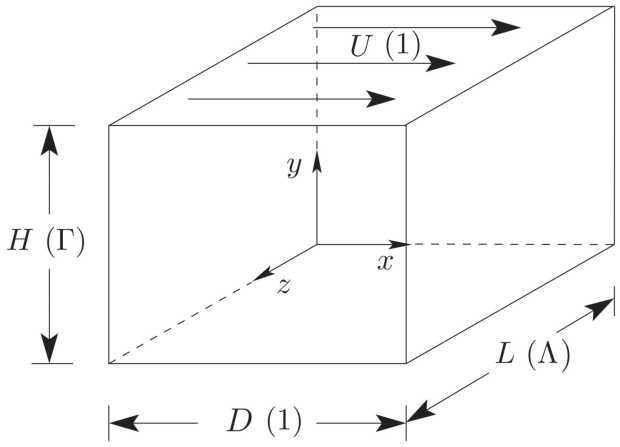

FIG. 1. Geometry and coordinates of the rectangular cuboidal cavity. Non-dimensional quantities are given in parentheses.

Scaling length, velocity, time, and pressure by D, U, D/U, and ρU^2, respectively, the governing Navier–Stokes and continuity equations read

$$\frac{\partial \boldsymbol{u}}{\partial t} + \boldsymbol{u}\cdot\nabla\boldsymbol{u} = -\nabla p + \frac{1}{\mathrm{Re}}\nabla^2\boldsymbol{u}, \tag{1a}$$

$$\nabla\cdot\boldsymbol{u} = 0, \tag{1b}$$

where $\boldsymbol{x} = (x, y, z)$, t, $\boldsymbol{u} = (u, v, w)$, and p denote the position vector, time, velocity vector field, and pressure field, respectively. The Reynolds number and the cross-sectional (Γ) and spanwise (Λ) aspect ratios, respectively, are defined as

$$\mathrm{Re} = \frac{UD}{\nu}, \quad \Gamma = \frac{H}{D}, \quad \Lambda = \frac{L}{D}. \tag{2}$$

Two different boundary conditions in the z direction are considered. For a finite-length cavity with $\Lambda < \infty$, the mathematical problem (1) is closed by no-slip and no-penetration boundary conditions on all walls,

$$\boldsymbol{u}(x = 0, 1) = \boldsymbol{0}, \tag{3a}$$

$$\boldsymbol{u}(y = 0) = \boldsymbol{0}, \quad \boldsymbol{u}(y = \Gamma) = \boldsymbol{e}_x, \tag{3b}$$

$$\boldsymbol{u}(z = 0, \Lambda) = \boldsymbol{0}, \tag{3c}$$

where $\boldsymbol{e}_x$ is the unit vector in the x direction. Another set of boundary conditions results if (3c) is replaced by periodic conditions in the z-direction,

$$\boldsymbol{u}(z = \lambda) = \boldsymbol{u}(z = 0), \tag{3d}$$

where λ is the spatial period. This set of boundary conditions applies to a cavity with an infinite span $\Lambda \to \infty$ when the flow is periodic in z.

We are interested in the streamline topology of the steady three-dimensional flow for these two types of boundary conditions, including fixed points, limit cycles, and regular vs chaotic streamlines. By investigating the influence of the spanwise length Λ on the flow topology, we aim at refining, extending, and quantifying the results obtained for this system by Ishii and Adachi (2006; 2010; 2011) and Ishii *et al.* (2012). In the case of periodic boundary conditions with the period λ ($\Lambda \to \infty$), we consider the steady three-dimensional flow slightly above the onset of periodic Taylor–Görtler vortices, which arise beyond the critical Reynolds number $\mathrm{Re}_c = 783.9$, fixing the wavelength to the critical value $\lambda_c = 0.406\,78$ of the linear stability problem (Albensoeder *et al.*, 2001b). Several Reynolds numbers for each set of boundary conditions and per each spanwise aspect ratio are investigated to shed light on the structure of the topological chaos and the way it is invading the system when the Reynolds number is increased.

III. NUMERICAL METHODS

A. Fluid flow

The flow field is calculated using a spectral-element method, which employs high-order Lagrange polynomials on Gauss–Legendre–Lobatto nodes defined in the $\mathbb{P}_N$ function space for the velocity and on Gauss–Legendre nodes defined in $\mathbb{P}_{N-2}$ for the pressure, where N denotes the polynomial order. The Navier–Stokes solver is implemented in the open-source code NEK5000 (Fischer *et al.*, 2008). The grid of elements is quadratically refined toward all no-slip walls, while it is uniform in the case of a periodic direction. The high-order stiffly stable scheme of Karniadakis *et al.* (1991) is adopted using third-order backward differentiation formulae for the linear operator and third-order explicit integration schemes for the non-linear terms. Polynomials of the seventh order are used in each direction, together with an over-integration method, which employs 12^3 Gaussian nodes per element in order to eliminate aliasing errors during computation of the integrals in the Galerkin weak formulation. The discontinuity in u at the cavity edges between stationary and moving walls is treated using a fifth-order polynomial expansion for the elements, which are located at the singular edges. A detailed study of the effect of this type of discontinuity on the numerical accuracy of spectral methods was provided by Botella and Peyret (1998) for the two-dimensional lid-driven cavity flow and by Albensoeder and Kuhlmann (2005) for the three-dimensional lid-driven cavity flow. Here, we limit ourselves to verify our code by comparison of the results we obtained with those given in Albensoeder and Kuhlmann (2005).

For all flow parameters investigated, the flow converges to a steady state. The simulations were terminated once the convergence criterion

$$\max_{\boldsymbol{x},i} \frac{|u_i(\boldsymbol{x},t) - u_i(\boldsymbol{x},t-\Delta t)|}{\Delta t} \le 10^{-7} \tag{4}$$

was satisfied. To make sure that non-solenoidal numerical errors have a negligible impact on the computation of the Lagrangian topology, each time step of the projection method is iterated until the residual of the continuity equation has become less than 10^{-12}. The minimization of divergence errors is important because such errors destroy the KAM structure of the flow and can lead to spurious attractors, which cannot exist in a true incompressible flow.

Correct implementation and grid convergence of the solver have been tested by comparing our simulation results for steady cubic and periodic three-dimensional lid-driven cavity flows with the benchmark data provided by Albensoeder and Kuhlmann (2005) for $\Gamma = 1$, $\lambda = 1$, and $\mathrm{Re} = 1000$ [by imposing the period $\lambda = 1$, three pairs of Taylor–Görtler vortices develop (Albensoeder and Kuhlmann, 2005)]. Results for both cases have been verified by comparing velocity profiles on the mirror-symmetry plane of the flow on which $w \equiv 0$. Figure 2 demonstrates a very good agreement between our simulations and the reference results, which can be achieved using ten elements per direction, corresponding to approximately 5×10^5 degrees of freedom. The flow fields employed for all topological analyses have been obtained for the finest resolution, distributing 20 high-order elements per unit length (full lines in Fig. 2).

B. Streamlines

The Lagrangian topological features of the flow are analyzed computing streamlines of the three-dimensional flow, which is steady according to criterion (4). Denoting with $\boldsymbol{X}(t)$ the location

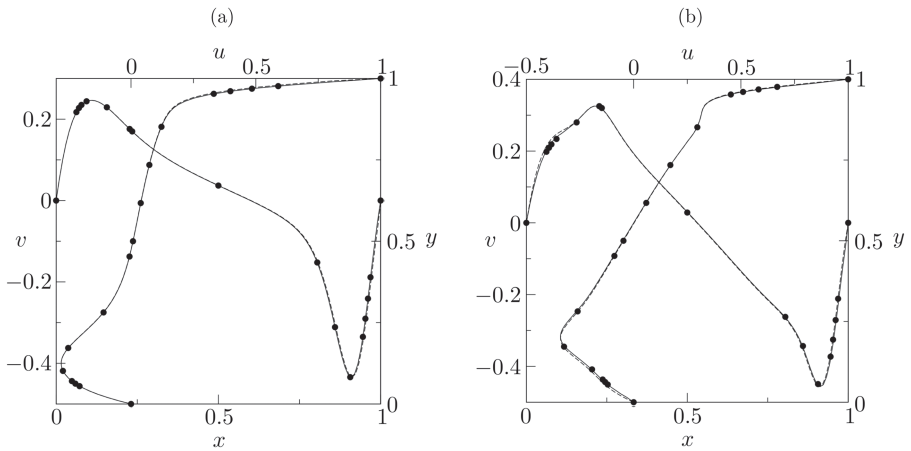

FIG. 2. Velocity profiles $u(0.5, y)$ and $v(x, 0.5)$ in the symmetry plane $z = \text{const.}$ in which $w = 0$. Shown are results for $\mathrm{Re} = 1000$ for (a) a cubic cavity with $\Gamma = \Lambda = 1$ and (b) an infinitely extended cavity ($\Lambda \to \infty$) with the period $\lambda = 1$. Simulation results from NEK5000 are shown as dashed (10^3 elements) and full lines (20^3 elements) in comparison with the benchmark data of Albensoeder and Kuhlmann (2005) (dots).

of an infinitesimal fluid element, the advection equation,

$$\frac{\mathrm{d}\boldsymbol{X}}{\mathrm{d}t} = \boldsymbol{u}\left[\boldsymbol{X}(t)\right], \tag{5}$$

is solved to compute the trajectory of a fluid element, coinciding with a streamline in a steady flow, where $\boldsymbol{X}_0 = \boldsymbol{X}(t=0)$ is its initial position.

The Runge–Kutta Dormand–Prince method (Dormand and Prince, 1980) is employed for the time discretization of (5). In this method, both the standard fourth- and fifth-order Runge–Kutta schemes are used. At each time step, the numerical integration error is estimated by comparison of the results obtained from the two schemes of a different order, i.e., $\|\boldsymbol{u}^{4\mathrm{th}} - \boldsymbol{u}^{5\mathrm{th}}\|_\infty$. If required, the time step Δt is reduced to satisfy the absolute and relative tolerances for the numerical error, both set to 10^{-7}. In addition to the approximation of the solution of (5) introduced by the time discretization, a further approximation results from interpolating in (5) the velocity field $\boldsymbol{u}$, which is computed beforehand on the Eulerian grid, and is now evaluated at the location of the fluid element $\boldsymbol{X}(t)$. For a first overview on the streamline topology, a linear interpolation is adopted. However, the regular periodic and quasiperiodic trajectories presented are computed more accurately using the spectral interpolant consistent with the spatial discretization employed in NEK5000.

IV. FINITE-LENGTH CAVITIES

Flows in finite-length cavities are investigated for a cubic cavity $(\Gamma, \Lambda) = (1, 1)$, a shallow cavity $(\Gamma, \Lambda) = (0.4, 1)$, and a long cavity $(\Gamma, \Lambda) = (1, 2)$. For all three cases, the flow topology is elaborated for $\mathrm{Re} = 100$, 200, 300, and 400.

A. Flow structure, symmetries, fixed points, and global transport

The structure of the two-dimensional flow in the (x, y)-plane is well known. The moving wall drives a main global vortex (primary flow). It separates from and re-attaches to the stationary walls, which make the two rigid bottom corners. The resulting two smaller separated vortices are often called secondary eddies. At a higher Reynolds number, a third separated vortex may arise on the stationary wall at $x = 0$ upstream of the moving wall and near the singular corner $(x, y) = (0, \Gamma)$. Apart from these main structures, an infinite sequence of viscous corner eddies (Moffatt, 1964) exists in the rigid corners made by the wall at $y = 0$ and the upstream and downstream stationary walls at $x = (0, 1)$ at any Reynolds number.

Even in the limit of vanishingly small Reynolds numbers, the flow in a cavity of finite length is weakly three-dimensional (Young *et al.*, 2004), an effect caused by the corners and edges made by the cavity end walls. As the Reynolds number and the strength of the primary flow increase, the presence of the no-slip end walls at $z = (0, \Lambda)$ induces another type of secondary flow via the Bödewadt (1940) mechanism. This secondary flow is caused by inertia, involves a significant spanwise velocity component w, and appears in the form of mirror-symmetrically placed ring-like vortices near the end walls (see, e.g., Sheu and Tsai, 2002). The mirror symmetry of the flow $[u, v, w](x, y, z - \Lambda/2) = [u, v, -w](x, y, -(z - \Lambda/2))$ is preserved for all Reynolds numbers considered. Since $w(z = \Lambda/2) = 0$, the mirror-symmetry plane $z = \Lambda/2$ defines a transport barrier to the fluid.

To visualize the structure of the end-wall-induced secondary vortex, Fig. 3 shows isosurfaces of $|w| = 0.1$ in one half of the cavity for $\mathrm{Re} = 300$. Dark- and light-gray isosurfaces indicate motion toward $(w = -0.1)$ and away from the end wall $(w = 0.1)$, respectively. Results are shown for all three geometries. In addition, in order to illustrate global circulation in the cavity, a streamline initiated at $(x, y, z) = (1/2, \Gamma/2, 0.001)$ is integrated until the streamline returns near its initialization point (dot). The (x, y)- and (y, z)-projections of this streamline are reported in the middle and right panels of Fig. 3. The flow is qualitatively similar for all three aspect ratios.

We first discuss the streamline structure in the midplane for $\Lambda = 1$. The Bödewadt mechanism drives a secondary flow, which is directed radially inward toward the axis of the main vortex flow near the end walls. Due to continuity, the fluid escapes from both end walls along the axis of the primary circulation and the two opposing streams meet at the midplane, creating a free stagnation point s_2. This type of stagnation point flow is related to the similarity solution of the Navier–Stokes equations provided by Wang (1985; 1987). Here, however, the swirl provided by the primary vortex makes the stagnation point s_2 a spiraling-out saddle focus. An example of the streamlines in the midplane $z = \Lambda/2$ is shown in Fig. 4(a) for $\mathrm{Re} = 300$ and $(\Gamma, \Lambda) = (1, 1)$. Due to the global structure of the end-wall-induced flow, similar, but spiraling-in, saddle foci s_1 are expected on each end wall. However, since all velocity components must vanish on $z = (0, \Lambda)$, all points on the end walls are stagnation points and the resulting spiraling-in saddle focus on the end wall is degenerate in this sense (Bödewadt, 1940). For a detailed analysis of the flow near a critical point on a stationary boundary, we refer to Brøns *et al.* (2001), who carried out a local Taylor expansion to characterize the flow near degenerate critical points where $\nabla \boldsymbol{u} = \boldsymbol{0}$.

The elliptic points of the two secondary corner vortices present in a corresponding two-dimensional cavity also become saddle foci s_4 and s_8 in the midplane of the three-dimensional finite-length cavity. If $|\partial w/\partial z|$ is large, such saddle foci may even vanish. Due to these end-wall-induced changes of the flow, the corner vortices are no longer separated but open to globally exchange fluid. If existent, we find the saddle focus s_4 near the corner $(x, y, z) = (1, 0, \Lambda/2)$ to be displaced away from the bottom wall as Re increases, while the saddle s_8 focus near $(x, y, z) = (0, 0, \Lambda/2)$ to be displaced toward the bottom wall (not shown), as compared to the position of the elliptic point in a two-dimensional flow. For the case shown in Fig. 4, the saddle focus s_4 in the bottom-right corner can be clearly identified. However, the free saddle focus s_8 expected in the bottom-left corner is not present. It does exist, however, for $\mathrm{Re} = 10$, but increasing Re to 100, it merges with the hyperbolic half-node s_6 on the bottom wall. After merging, s_6 has become a degenerate stable half-node, hence degenerate sink in the (x, y) subspace. The hyperbolic separation points $s_{3,5,6,7}$ in the two-dimensional cavity flow preserve their qualitative structure in the midplane of the three-dimensional flow [Fig. 4(a)], but their locations depend on Re.

From the transport in the midplane, the two-dimensional unstable manifold of s_2 is heteroclinically connected with the two-dimensional stable manifolds of s_4 and s_6. The two-dimensional

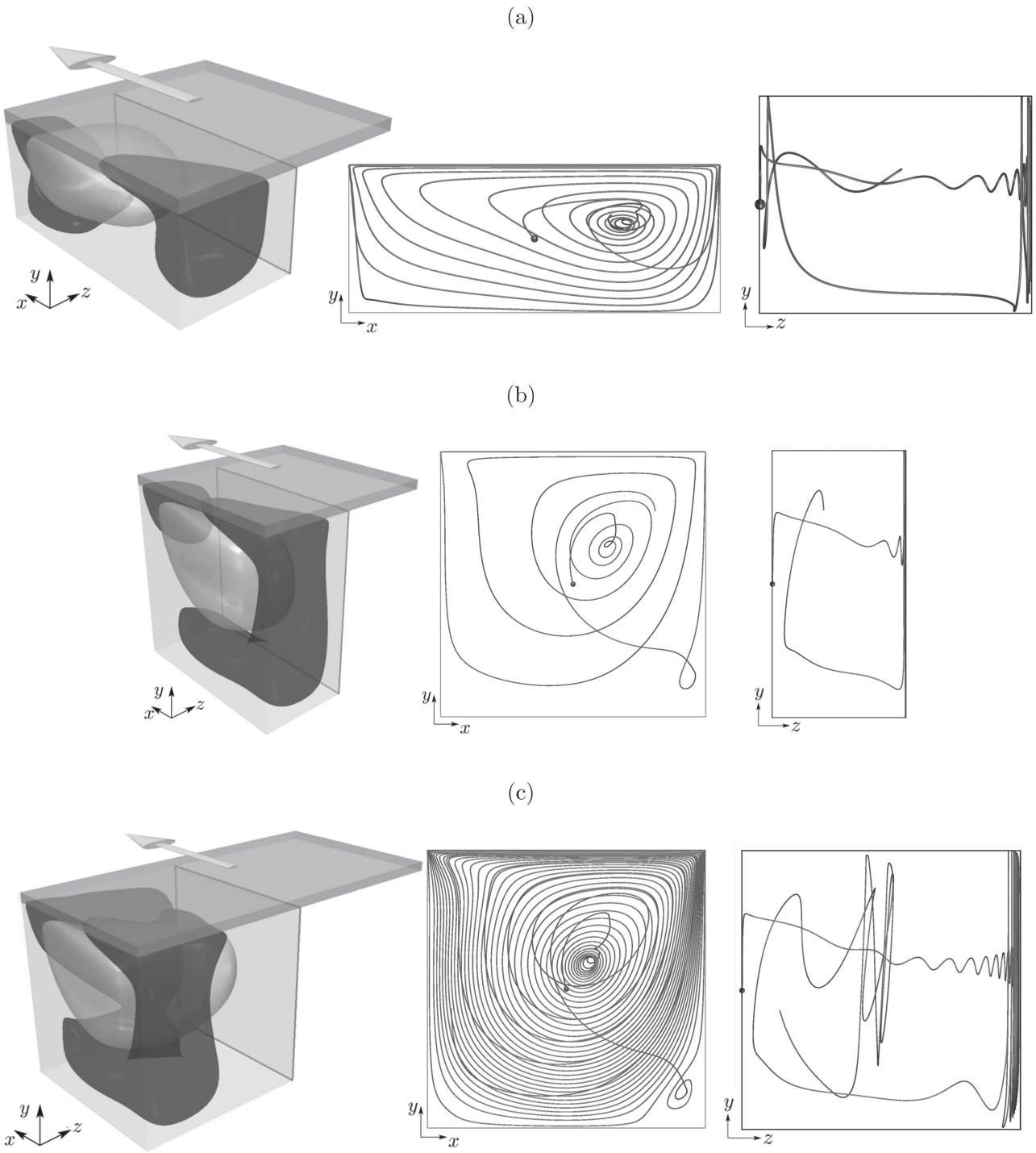

FIG. 3. Secondary flow for Re $= 300$ (left side) characterized by isosurfaces of $w = 0.1$ (light gray) and $w = -0.1$ (dark gray) and (x, y)- and (y, z)-projections, middle and right panels, respectively, of a streamline initialized at $(x, y, z) = (1/2, \Gamma/2, 0.001)$ and integrated until a streamline returns near its initialization point (dot). The geometrical parameters of the cavity flows are $(\Gamma, \Lambda) = (0.4, 1)$ (a), $(1, 1)$ (b), and $(1, 2)$ (c) Shown is one half of the symmetric cavity.

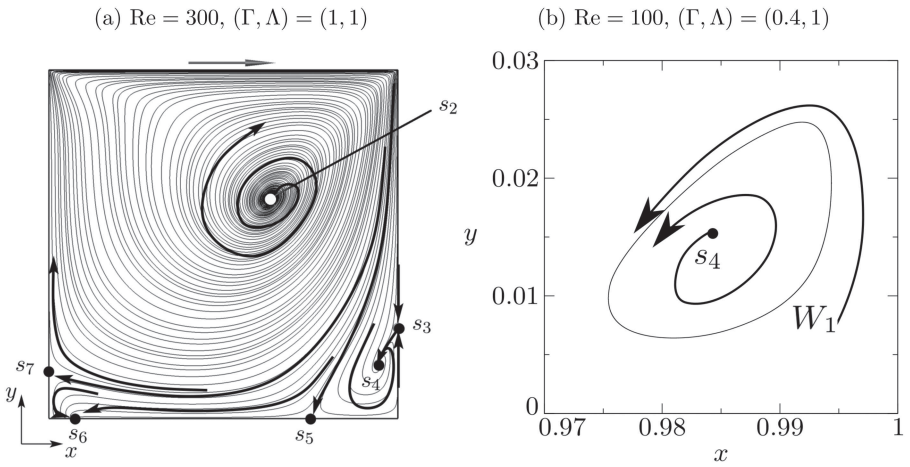

FIG. 4. (a) Streamlines on the midplane $z = \Lambda/2$ for $\mathrm{Re} = 300$ and $(\Gamma, \Lambda) = (1, 1)$ (thin lines). The spiraling-out and spiraling-in saddle foci s_2 and s_4, respectively, and the critical points on the wall $s_{3,5,6,7}$ are indicated by dots. (b) Spiraling-in limit cycle W_1 and spiraling-out saddle focus s_4 on the midplane $z = \Lambda/2$ for $\mathrm{Re} = 100$ and $(\Gamma, \Lambda) = (0.4, 1)$. The solid bold lines and the arrows are guides to the eyes to highlight the flow direction and are not computed streamlines.

stable manifolds of s_4 and s_6 are bounded in the midplane by the one-dimensional stable manifolds of s_5 and s_7, which are also heteroclinically connected with s_2. Hence, the two-dimensional unstable manifold of s_2 in the midplane $z = \Lambda/2$ [Fig. 4(a)] is made of the union of the two-dimensional stable manifolds of the spiraling-in saddle focus s_4 and the degenerate half-node s_6. Wall streamlines, critical points, and separation lines have been analyzed by Sheu and Tsai (2002).

The fluid transport to and from the midplane for $\Lambda = 1$ is sketched in Fig. 5. The transport is mainly organized along the stable and unstable one-dimensional manifolds of the saddle focus in the midplane (s_2) and those on the end walls (s_1), respectively, which are not heteroclinically connected. Fluid originating from the vicinity of the half-saddle foci s_1 on the end walls is transported in the z direction along the unstable manifold of s_1 toward s_2 in a spiraling fashion (white arrow from $z = \Lambda$ to $z = \Lambda/2$). From there, it moves radially away from s_2, being separated into two streams (shown in light gray). One is approaching the half-node s_6, while the other one is approaching the saddle focus s_4. Near the edges $(x, y) = (0, 0)$ and $(1, 0)$, each of the two streams symmetrically splits into two and leaves the midplane in positive and negative z directions to reach the two end walls (white arrows from $z = \Lambda/2$ to $z = \Lambda$), near which they are again interwoven near the two-dimensional stable manifold of s_1 (shown in dark gray). The broken heteroclinic connection between s_1 and s_2 and the three-dimensional splitting and merging near the midplane and the end walls, respectively, provides the basic mechanism for the chaotic mixing in the three-dimensional cavity. The splitting, folding, and merging correspond to the typical mechanism of a baker map (Tél and Gruiz, 2006).

The evolution of the character of the stationary points and their connectedness with Re can be intricate. For instance, for $\mathrm{Re} < 4$, the two saddle foci s_1 and s_2 are heteroclinically connected. However, for $\mathrm{Re} \gtrsim 10$, we find that the heteroclinic connection is broken. Even though the one-dimensional unstable manifold of s_1 approaches the stationary point s_2, it clearly does not end on s_2 for $\mathrm{Re} \geq 100$. Moreover, the saddle focus s_4 undergoes several changes [Fig. 4(a)]: In the cubic cavity, $(\Gamma, \Lambda) = (1, 1)$, it is absent for moderate Reynolds numbers and

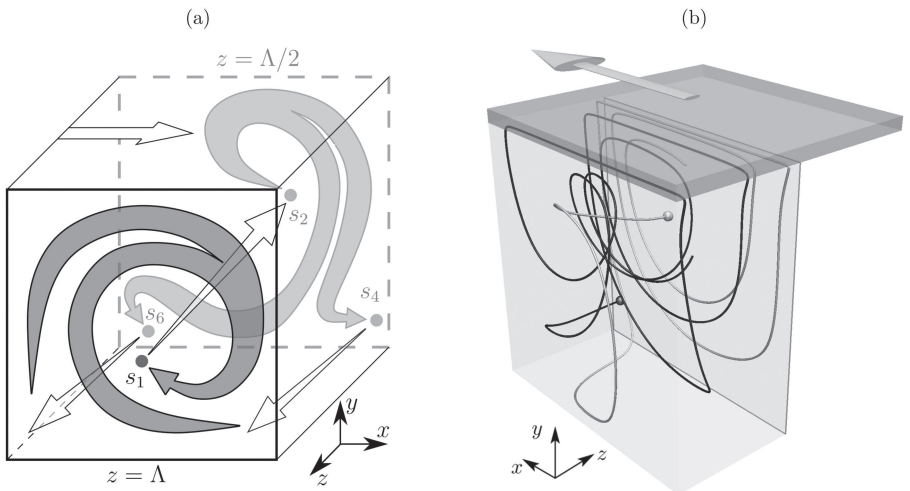

FIG. 5. (a) Sketch of the main transport path for $\Lambda = 1$ and $z \in [\Lambda/2, \Lambda]$: Stream splitting in the midplane (light gray) and stream merging near each end wall (dark gray). The transport between the two planes due to the secondary flow is indicated symbolically by the white arrows inside the cavity. Fixed points are shown by dots and labels. The arrow at $y = \Gamma$ indicates the wall motion. The bold square indicates one of the two end walls, whereas the thick dashed light gray square represents the midplane. (b) Streamline originating from s_4 (dark gray dot) and integrated forward in time (dark gray line) and streamline originating from s_2 (light gray dot) and integrated backward in time (light gray line) for $\mathrm{Re} = 300$ and $(\Gamma, \Lambda) = (1, 1)$.

only appears for $\mathrm{Re} \geq 300$. The existence of s_4 at moderate Reynolds is thus understood as a result of the increased inertia of the flow, which produces a sufficiently large vorticity ω_z in the midplane near the corner. For the geometry $(\Gamma, \Lambda) = (0.4, 1)$, we find the saddle focus s_4 even changes from spiraling-in to spiraling-out when Re is increased. This is demonstrated in Fig. 4(b). Here, the spiraling-out saddle focus is created at the expense of a limit cycle W_1, which is spiraling-in from both sides over the midplane. At higher Reynolds numbers, W_1 vanishes and s_4 turns into a spiraling-in saddle focus. These topological features are consistent with the results of Chiang and Sheu (1997).

A different streamline topology is found when considering a long cavity with $\Lambda = 2$ and $\mathrm{Re} \geq 300$. As the spanwise aspect ratio Λ increases, the flow near the midplane approaches a two-dimensional flow and the spiraling streamlines at $z = \Lambda/2$ become very dense. As shown in Fig. 6(a), we find that the outward spiraling streamlines (gray) approach a saddle limit cycle V_1 on $z = \Lambda/2$ [gray in Fig. 6(b)]. This limit cycle is radially approached from outside by spiraling-in streamlines (not shown) originating from a second saddle limit cycle V_2 in the midplane [gray in Fig. 6(c)]. The complementary part of the unstable manifold of V_2 splits into streamlines, which spiral outward, either into the spiraling-in saddle focus s_4 or into a spiraling-in saddle focus s_{10}, found only for $\Lambda = 2$ [see Figs. 6(a) and 6(b)]. The stable manifolds of s_4 and s_{10} are separated by the stable one-dimensional manifold of s_5 on the bottom wall (not shown). A spiraling-out free saddle focus, s_8, emerges for $\Lambda = 2$ near the bottom-left corner. This saddle focus spirals out, and its unstable manifold extends tightly along the cavity walls, including the moving lid, and joins in a spiraling fashion with part of the unstable manifold of V_2 to become the stable manifold of s_4 [see Fig. 6(c)]. The unstable manifold of the separation point s_6 (not shown) on the bottom wall separates the unstable manifold of s_8 and the unstable manifold of V_2. Hence, all the streamlines originating from s_8 and V_2 spiral into s_4 or s_{10} from where the fluid is released to the bulk. The splitting and merging of manifolds are similar to what happens near the midplane and the end walls described for $\Lambda = 1$ [Fig. 5(a)] and contribute to the streamline chaos.

While Moffatt eddies can clearly be resolved for the two-dimensional cavity flow, we did not find any indication of Moffatt eddies in the midplane of the three-dimensional flow for $\Lambda = 1$. The absence of viscous corner eddies for the cubical cavity ($\Gamma = \Lambda = 1$) is consistent with their absence in the Stokes eigenmodes spectrally computed by Leriche and Labrosse (2011). On the other hand, the flow for $\Lambda = 2$ exhibits a novel saddle focus s_{10} in the midplane located close to the corner made by the bottom and the downstream wall. This critical point is a precursor of the Moffatt eddies, which emerge in the midplane upon an increase of the spanwise aspect ratio.

Similar as Ishii and Adachi (2010) for $\Lambda = 6.55$ and consistent with the spiraling-out of s_8, we find that w changes its sign near the midplane and the upstream corner. The isosurfaces for $w = 0.0001$ (dark gray) and $w = -0.0001$ (light gray) are shown in Fig. 7 for $\mathrm{Re} = 300$ (a) and $\mathrm{Re} = 400$ (b). Figure 8 depicts the projection onto the (x, z)-plane of the unstable manifold of s_8 and s_4 [Figs. 8(a) and 8(c)] and the stable manifold of s_{10} [Fig. 8(b)]. Their unstable manifolds extend to the end walls very close and almost parallel to the corresponding cavity edge.

Finally, considering the lid-driven cavity is ever since a numerical benchmark for computational fluid dynamics, quantitative numerical data are of high interest for code verification and benchmarking of three-dimensional flows. For that purpose, we provide in Table I numerical data for the locations of the two saddle foci s_2 and s_4 in the midplane as a function of Re, Γ, and Λ. Furthermore, the corresponding eigenvalues and eigenvectors of the velocity-gradient tensor $\nabla \boldsymbol{u}$ evaluated at the locations of $s_{2,4}$ are provided in Tables I and II, respectively.

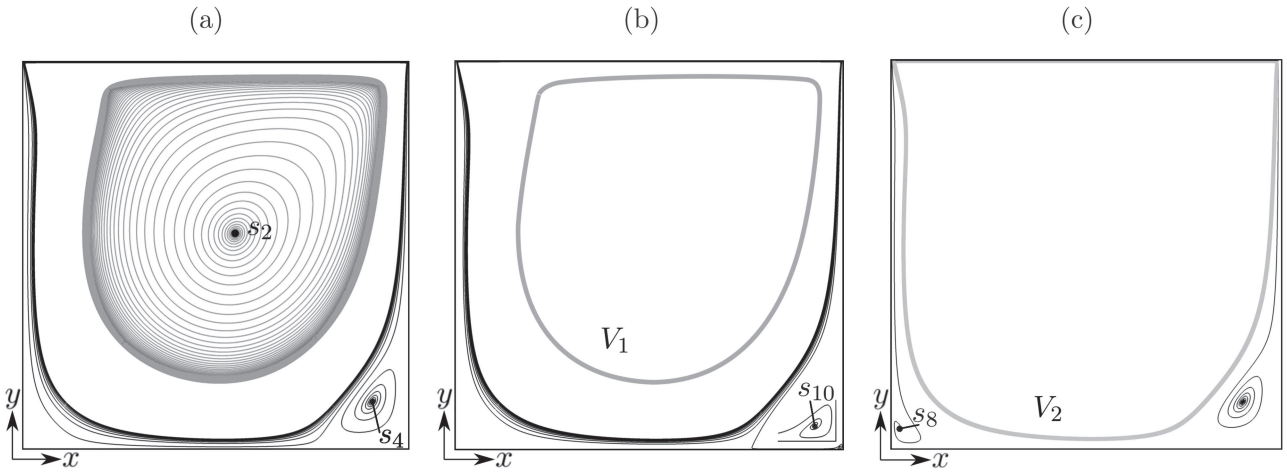

FIG. 6. Streamline pattern in the symmetry plane at $z = \Lambda/2$ for $\mathrm{Re} = 400$, $\Gamma = 1$, and $\Lambda = 2$. The two saddle limit cycles V_1 (gray) and V_2 (black) are shown as thick lines. (a) Streamline (gray) originating from s_2 and spiraling out toward the limit cycle V_1 (not shown) and streamline (black) originating from V_2 (black) and spiraling out toward the saddle focus s_4. (b) Limit cycle V_1 (gray) and streamline (black) originating from V_2 and spiraling out toward the saddle focus s_{10}. Near the bottom-right corner, a closeup of the streamline is depicted. (c) Limit cycle V_2 (gray) and streamline (black) originating from s_8 and spiraling out toward the saddle focus s_4.

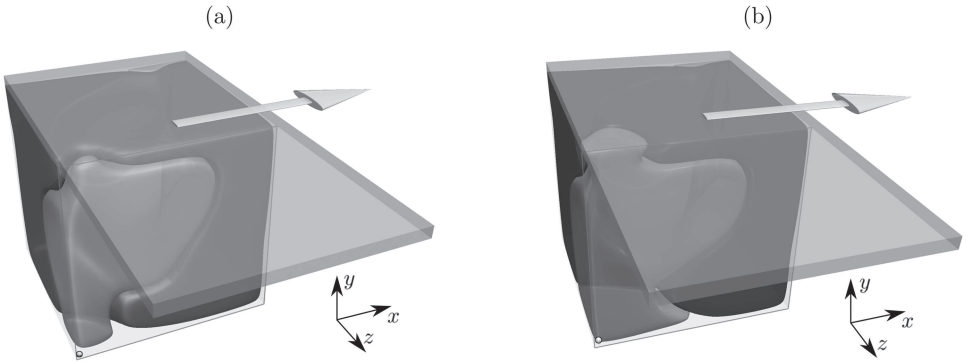

FIG. 7. Isosurface of $w = 0.0001$ (dark gray) and $w = -0.0001$ (light gray) indicating the flow direction away from the midplane near the upstream corner for $\mathrm{Re} = 300$ (a) and $\mathrm{Re} = 400$ (b). The white dot denotes the saddle focus s_8.

B. KAM tori and chaotic sea

1. General behavior

When the Reynolds number is small, and a heteroclinic connection between s_1 and s_2 exists, most streamlines are regular. The regular region arises as a pair of sets of Kolmogorov–Arnold–Moser (KAM) tori, which are mirror-symmetric with respect to the midplane $z = \Lambda/2$. The emergence of these regular regions in the form of invariant tori is described by the KAM theorem and is a direct consequence of the local Hamiltonian nature of the three-dimensional steady flow. Merely, a thin layer of chaotic streamlines is found to exist around the heteroclinic connection between s_1 and s_2; hence, the curvilinear axis of the outermost KAM torus is well approximated by the one-dimensional stable manifold of s_2 and the one-dimensional unstable manifold of s_1. This slender tube of chaotic streamlines extends to thin layers, covering the midplane and all solid walls. The origin of this chaotic skin is related to partitioning of the fluid in the midplane, whenever $\mathrm{Re} \neq 0$, which is organized by the singular points in the midplane near s_4 and s_6. Moreover, the local flow near the trihedral corners, for which Scott (2013) found non-periodic streamlines of the least rapidly decaying Stokes-flow modes as the apex of the corner is approached, contributes, too.

As the Reynolds number increases beyond $\mathrm{Re} \gtrsim 4$, the heteroclinic connection between s_1 and s_2 is broken. The broken connection tends to thicken the chaotic layer. Moreover, the splitting of the outward spiraling motion in the midplane into two streams, one near each bottom edge, in each cavity half continues to contribute to the chaos. In particular, the one-dimensional unstable manifold of s_4 does play an important role since highly strained fluid from the singular edges at the midplane arrives near s_4 from where it is ejected in the third (z) dimension (cf. Fig. 5). For even larger Reynolds numbers, the chaotic layer grows further, the KAM tori shrink, and the flow topology becomes more complex due to resonance phenomena within the KAM tori, which are occupied by quasiperiodic, i.e., non-resonant streamlines. At a resonance, a streamline winding on a KAM torus reconnects with itself. As a consequence of the Hamiltonian nature of the three-dimensional steady flow and the Poincaré–Birkhoff theorem, the torus breaks down into elliptic and hyperbolic closed streamlines (see, e.g., Schuster, 2005). The elliptic closed streamlines are embedded in newly created KAM tori, which are surrounded by a chaotic layer organized around the hyperbolic

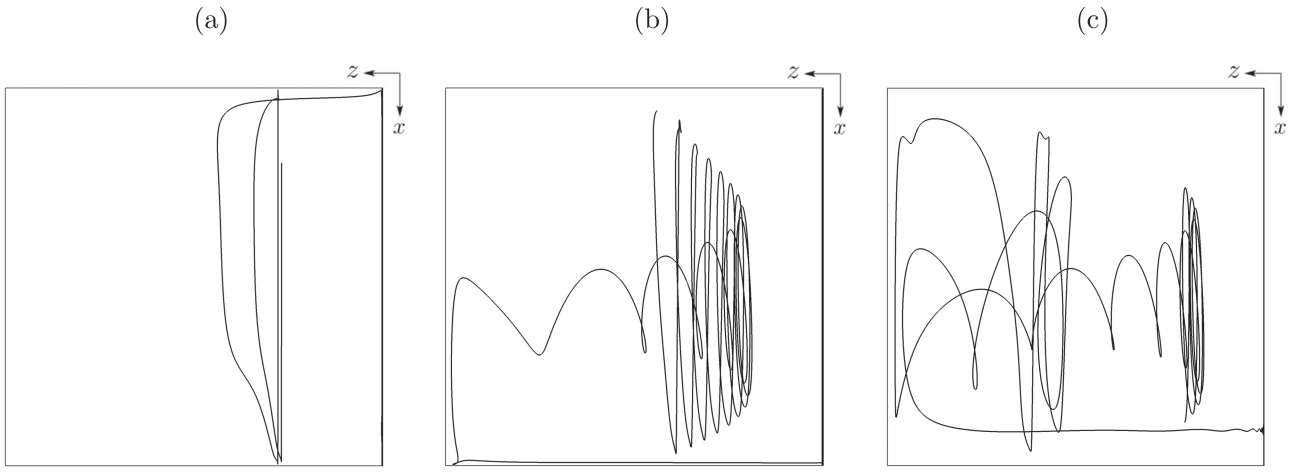

FIG. 8. Projection of a streamline onto the plane (x, z) showing the global connection of the free spiraling-in saddle focus s_8 (a), the spiraling-out saddle focus s_{10} (b), and the spiraling-in saddle focus s_4 (c). The midplane is on the right side.

TABLE I. Locations of the saddle foci $s_{2,4}$ on $z = \Lambda/2$ and corresponding eigenvalues of the velocity-gradient tensor.

Λ	Γ	Re	$\boldsymbol{x}_{s_2} = (x_{s_2}, y_{s_2})$	$\lambda_{1,2}^{s_2}$	$\lambda_3^{s_2}$	$\boldsymbol{x}_{s_4}$	$\lambda_{1,2}^{s_4}$	$\lambda_3^{s_4}$
1	0.4	100	(0.6892, 0.2633)	0.058 ± 1.641i	-0.116	(0.9843, 0.0153)	0.003 ± 0.025i	-0.006
		200	(0.7280, 0.2521)	0.104 ± 2.089i	-0.208	(0.9850, 0.0207)	-0.005 ± 0.047i	0.094
		300	(0.7346, 0.2383)	0.111 ± 2.021i	-0.222	(0.9836, 0.0264)	-0.011 ± 0.079i	0.022
		400	(0.7292, 0.2254)	0.093 ± 1.847i	-0.186	(0.9820, 0.0320)	-0.026 ± 0.119i	0.052
1	1	100	(0.6167, 0.7588)	0.122 ± 1.381i	-0.244			
		200	(0.6453, 0.6997)	0.109 ± 0.982i	-0.218			
		300	(0.6348, 0.6293)	0.082 ± 0.772i	-0.164	(0.9478, 0.1577)	-0.027 ± 0.067i	0.054
		400	(0.6221, 0.5751)	0.066 ± 0.663i	-0.132	(0.9283, 0.1520)	-0.037 ± 0.142i	0.074
2	1	100	(0.6140, 0.7396)	0.026 ± 1.474i	-0.052	(0.9528, 0.0736)	-0.002 ± 0.014i	0.004
		200	(0.6022, 0.6525)	0.025 ± 1.094i	-0.050	(0.9317, 0.1202)	-0.009 ± 0.053i	0.018
		300	(0.5712, 0.5862)	0.028 ± 0.947i	-0.056	(0.9145, 0.1243)	-0.008 ± 0.113i	0.016
		400	(0.5508, 0.5564)	0.032 ± 0.814i	-0.064	(0.9058, 0.1214)	-0.009 ± 0.164i	0.018

closed streamlines. To characterize the flow structures, we investigate the evolution of the KAM tori as a function of the Reynolds number. KAM tori are reconstructed for Re = 100, 200, 300, and 400 in the shallow ($\Gamma = 0.4$, $\Lambda = 1$), the cubic ($\Gamma = \Lambda = 1$), and the slender cavity ($\Gamma = 1$, $\Lambda = 2$).

2. Computing KAM tori

To characterize regular and chaotic regions in the flow, 100 fluid elements were evenly distributed at $t = 0$ along the line $(x, y) = (x_{s_2}, y_{s_2})$ within one half of the cavity $z \in [0, \Lambda/2]$. Streamlines were obtained integrating the advection equation from $t = 0$

TABLE II. Normalized eigenvectors of the velocity-gradient tensor at the two saddle foci $s_{2,4}$ on $z = \Lambda/2$.

Λ	Γ	Re	$\boldsymbol{v}_{1,2}^{s_2}$	$\boldsymbol{v}_3^{s_2}$
1	0.4	100	$(0.948,\ -0.008 \pm 0.318\text{i},\ 0.000)^{\mathrm{T}}$	$(0.000,\ 0.000,\ 1.000)^{\mathrm{T}}$
		200	$(0.899,\ -0.010 \pm 0.437\text{i},\ 0.000)^{\mathrm{T}}$	$(0.000,\ 0.000,\ 1.000)^{\mathrm{T}}$
		300	$(0.876,\ -0.007 \pm 0.481\text{i},\ 0.000)^{\mathrm{T}}$	$(0.000,\ 0.000,\ 1.000)^{\mathrm{T}}$
		400	$(0.871,\ -0.018 \pm 0.491\text{i},\ 0.000)^{\mathrm{T}}$	$(0.000,\ 0.000,\ 1.000)^{\mathrm{T}}$
1	1	100	$(0.803,\ 0.069 \pm 0.591\text{i},\ 0.000)^{\mathrm{T}}$	$(0.000,\ 0.000,\ 1.000)^{\mathrm{T}}$
		200	$(0.721,\ 0.202 \pm 0.662\text{i},\ 0.000)^{\mathrm{T}}$	$(0.000,\ 0.000,\ 1.000)^{\mathrm{T}}$
		300	$(0.237 \mp 0.657\text{i},\ 0.716,\ 0.000)^{\mathrm{T}}$	$(0.000,\ 0.000,\ 1.000)^{\mathrm{T}}$
		400	$(0.216 \mp 0.655\text{i},\ 0.724,\ 0.000)^{\mathrm{T}}$	$(0.000,\ 0.000,\ 1.000)^{\mathrm{T}}$
2	1	100	$(0.775,\ 0.106 \pm 0.623\text{i},\ 0.000)^{\mathrm{T}}$	$(0.000,\ 0.000,\ 1.000)^{\mathrm{T}}$
		200	$(0.719,\ 0.180 \pm 0.671\text{i},\ 0.000)^{\mathrm{T}}$	$(0.000,\ 0.000,\ 1.000)^{\mathrm{T}}$
		300	$(0.122 \mp 0.694\text{i},\ 0.709,\ 0.000)^{\mathrm{T}}$	$(0.000,\ 0.000,\ 1.000)^{\mathrm{T}}$
		400	$(0.086 \mp 0.683\text{i},\ 0.725,\ 0.000)^{\mathrm{T}}$	$(0.000,\ 0.000,\ 1.000)^{\mathrm{T}}$
Λ	Γ	Re	$\boldsymbol{v}_{1,2}^{s_4}$	$\boldsymbol{v}_3^{s_4}$
1	0.4	100	$(0.727,\ 0.499 \mp 0.472\text{i},\ 0.000)^{\mathrm{T}}$	$(0.000,\ 0.000,\ 1.000)^{\mathrm{T}}$
		200	$(0.415 \pm 0.497\text{i},\ 0.762,\ 0.000)^{\mathrm{T}}$	$(0.000,\ 0.000,\ 1.000)^{\mathrm{T}}$
		300	$(0.354 \pm 0.473\text{i},\ 0.806,\ 0.000)^{\mathrm{T}}$	$(0.000,\ 0.000,\ 1.000)^{\mathrm{T}}$
		400	$(0.354 \pm 0.443\text{i},\ 0.824,\ 0.000)^{\mathrm{T}}$	$(0.000,\ 0.000,\ 1.000)^{\mathrm{T}}$
1	1	100		
		200		
		300	$(0.297 \pm 0.378\text{i},\ 0.876,\ 0.000)^{\mathrm{T}}$	$(0.000,\ 0.000,\ 1.000)^{\mathrm{T}}$
		400	$(0.319 \pm 0.448\text{i},\ 0.835,\ 0.000)^{\mathrm{T}}$	$(0.000,\ 0.000,\ 1.000)^{\mathrm{T}}$
2	1	100	$(0.341 \pm 0.481\text{i},\ 0.807,\ 0.000)^{\mathrm{T}}$	$(0.000,\ 0.000,\ 1.000)^{\mathrm{T}}$
		200	$(0.317 \pm 0.460\text{i},\ 0.829,\ 0.000)^{\mathrm{T}}$	$(0.000,\ 0.000,\ 1.000)^{\mathrm{T}}$
		300	$(0.330 \pm 0.497\text{i},\ 0.802,\ 0.000)^{\mathrm{T}}$	$(0.000,\ 0.000,\ 1.000)^{\mathrm{T}}$
		400	$(0.347 \pm 0.523\text{i},\ 0.778,\ 0.000)^{\mathrm{T}}$	$(0.000,\ 0.000,\ 1.000)^{\mathrm{T}}$

to $t = 200$ using a linear interpolation of $\boldsymbol{u}$ between grid points. In case the Poincaré section of the streamline on the plane $x = 1/2$ showed an erratic behavior, the streamline was assigned to the chaotic sea [light-gray dots in subfigures (a) of Figs. 9–19]. The existence of KAM tori was probed by dedicated initial conditions in those regions on the Poincaré plane $x = 1/2$ not visited by chaotic streamlines. Once a regular streamline was found, the same streamline is re-computed using the more accurate spectral interpolation. Moreover, for computing the regular regions, the relative and absolute tolerances of the Dormand–Prince method are both reduced to 10^{-9}. The periodic streamlines that result when the cross-sectional area of the KAM tori tends to zero are then identified, for each set of KAM tori, by computing the associated elliptic fixed points on the Poincaré plane $x = 1/2$ by means of the Newton–Raphson iteration, with an absolute tolerance of 10^{-3}. The coordinates of the elliptic fixed points of the Poincaré map on $x = 1/2$ defining the closed streamlines are listed in Tables III–V. Also given are the periods τ of the closed streamlines and their minimum distance Δ from the walls. The wall closest to the regular regions is always the moving wall at $y = \Gamma$. The minimum distances from the walls are also given for the largest quasiperiodic orbits identified per each

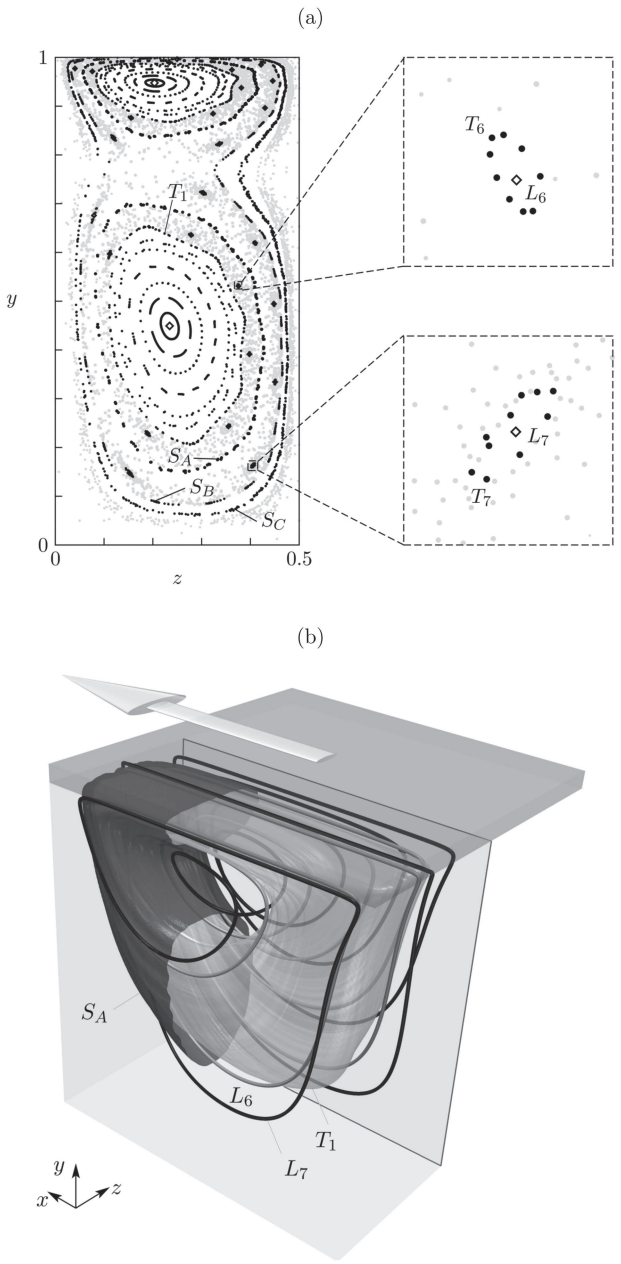

FIG. 9. (a) Poincaré section on $x = 1/2$ for Re $= 100$, $\Gamma = 1$, and $\Lambda = 1$. Gray dots, black dots, crosses, and diamonds indicate chaotic, regular, and closed streamlines, respectively. (b) Three-dimensional reconstruction of the transport barrier S_A (dark gray), 6- and 7-periodic closed streamlines, L_6 and L_7, respectively, and the outermost surface of the main KAM torus T_1 (light gray).

TABLE III. Characterization of periodic streamlines L, transport barriers S and of quasiperiodic streamlines on the largest reconstructible KAM tori T by their minimum distance Δ from the moving wall for $(\Gamma, \Lambda) = (1, 1)$. In addition, the locations on the plane $x = 1/2$ (fixed point) of the closed streamlines L_j are provided, as well as their periods τ. Only one single arbitrary fixed point is given for each closed streamline.

Λ	Γ	Re	KAM/ streamline	τ	Δ	Fixed point (y, z)
1	1	100	T_1		0.0134	
			L_1	6.782	0.0513	(0.449, 0.234)
			T_6		0.0098	
			L_6	51.359	0.0105	(0.392, 0.398)
			T_7		0.0041	
			L_7	78.290	0.0043	(0.722, 0.303)
			S_A		0.0061	
			S_B		0.0019	
			S_C		0.0011	
		200	T_1		0.0231	
			L_1	7.575	0.0469	(0.372, 0.210)
			T_4		0.0151	
			L_4	35.650	0.0162	(0.346, 0.383)
			T_7		0.0192	
			L_7	55.953	0.0208	(0.297, 0.304)
			T_{12}		0.0079	
			L_{12}	107.875	0.0081	(0.157, 0.365)
		300	T_1		0.0341	
			L_1	8.180	0.0442	(0.306, 0.188)
			T_5		0.0291	
			L_5	41.299	0.0294	(0.305, 0.239)
			T_7		0.0328	
			L_7	57.395	0.0337	(0.285, 0.220)
			T_{20}		0.0268	
			L_{20}	165.207	0.0273	(0.269, 0.179)
			S_A		0.0322	
			S_B		0.0303	
		400				

TABLE IV. Characterization of periodic streamlines L, transport barriers S and of quasiperiodic streamlines on the largest reconstructible KAM tori T by their minimum distance Δ from the moving wall for $(\Gamma, \Lambda) = (0.4, 1)$. In addition, the locations on the plane $x = 3/4$ (fixed point) of the closed streamlines L_j are provided, as well as their periods τ. Only one single arbitrary fixed point is given for each closed streamline.

Λ	Γ	Re	KAM/ streamline	τ	Δ	Fixed point (y, z)
1	0.4	100	T_1		0.0121	
			L_1	5.065	0.0388	(0.141, 0.157)
			T_{12}		0.0120	
			L_{12}	67.144	0.0122	(0.141, 0.288)
			T_{15}		0.0060	
			L_{15}	91.029	0.0064	(0.146, 0.349)
			T_{19}		0.0021	
			L_{19}	126.744	0.0023	(0.143, 0.408)
			T_{20}		0.0021	
			L_{20}	137.181	0.0020	(0.148, 0.420)
			T_{22}		0.0011	
			L_{22}	160.634	0.0013	(0.132, 0.439)
			T_{25}		0.0009	
			L_{25}	205.852	0.0009	(0.169, 0.453)
			S_A		0.0059	
		200	T_1		0.0221	
			L_1	4.069	0.0389	(0.124, 0.146)
			T_6		0.0198	
			L_6	32.005	0.0211	(0.370, 0.210)
			T_7		0.0126	
			L_7	38.351	0.0139	(0.125, 0.283)
			T_8		0.0068	
			L_8	44.566	0.0088	(0.131, 0.324)
			T_{13}		0.0158	
			L_{13}	69.688	0.0161	(0.137, 0.253)
			S_A		0.0182	
			S_B		0.0148	
			S_C		0.0119	
		300	T_1		0.0271	
			L_1	5.228	0.0432	(0.115, 0.132)
			T_5		0.0188	
			L_5	25.416	0.0190	(0.111, 0.235)
			T_9		0.0248	
			L_9	46.176	0.0251	(0.110, 0.190)
			T_{14}		0.0239	
			L_{14}	71.811	0.0241	(0.110, 0.200)
			T_{25}		0.0177	
			L_{25}	127.632	0.0179	(0.107, 0.227)
		400	T_1		0.0432	
			L_1	4.890	0.0441	(0.116, 0.111)
			T_3		0.0361	
			L_3	14.672	0.0383	(0.099, 0.121)
			T_4		0.0201	
			L_4	19.701	0.0239	(0.137, 0.076)
			T_7		0.0299	
			L_7	34.279	0.0302	(0.091, 0.143)
			T_{16}		0.0348	
			L_{16}	78.234	0.0350	(0.105, 0.131)
			T_{13}		0.0338	
			L_{13}	63.596	0.0340	(0.101, 0.132)
			S_A		0.0358	

set of KAM tori. The cross sections of the regular regions visualized in this manner are presented in subfigures (b) of Figs. 9–19. The closed streamlines and the largest reconstructible KAM tori are denoted L_j and T_j, respectively, where the subscript j indicates their periodicity.

Tables III–V and IX (further below for infinitely extended cavities) provide quantitative data for the location of the Lagrangian topology and can be employed for benchmarking. Moreover, the characterization of the minimum distance from the walls of the KAM tori and the corresponding elliptic streamlines is a key geometric parameter for the motion of nearly neutrally buoyant particles with finite size. The finite size of a particle becomes important for its motion near the boundaries, where the steric effect introduces a dissipation mechanism in the particle dynamics (Hofmann and Kuhlmann, 2011; Romanò and Kuhlmann, 2016; 2017a). If the particle radius is comparable to Δ (see Romanò *et al.*, 2019 for a detailed discussion), the particles can be transferred from chaotic

TABLE V. Characterization of periodic streamlines L, transport barriers S and of quasiperiodic streamlines on the largest reconstructible KAM tori T by their minimum distance Δ from the moving wall for $(\Gamma, \Lambda) = (1, 2)$. In addition, the locations on the plane $x = 1/2$ (fixed point) of the closed streamlines L_j are provided, as well as their periods τ_j. Only one single arbitrary fixed point is given for each closed streamline.

Λ	Γ	Re	KAM/ streamline	τ	Δ	Fixed point (y, z)
2	1	100	T_1		0.0252	
			L_1	6.799	0.0488	(0.423, 0.284)
			T_7		0.0159	
			L_7	52.657	0.0182	(0.346, 0.468)
			T_8		0.0110	
			L_8	64.262	0.0114	(0.313, 0.538)
			T_9		0.0081	
			L_9	75.904	0.0083	(0.287, 0.587)
			T_{36}		0.0077	
			L_{36}	303.417	0.0078	(0.209, 0.541)
			S_A		0.0139	
		200	T_1		0.0311	
			L_1	7.098	0.0459	(0.366, 0.238)
		300	T_1		0.0313	
			L_1	7.393	0.0430	(0.319, 0.194)
		400	T_{1M}		0.0022	
			L_{1M}	13.106	0.0118	(0.097, 0.896)

to regular regions of the flow and get trapped in or near the KAM tori. This way, small particles with the radius $a \in [\approx \Delta/2, \Delta]$ can be attracted to periodic or quasiperiodic orbits. For instance, for $\mathrm{Re} = 100$, $\Gamma = \Lambda = 1$ spherical particles with $a \in [0.002, 0.004] \times D$ can lead to finite-size coherent structures of period 7.

Once a quasiperiodic streamline on the largest identifiable KAM torus has been computed, the three-dimensional KAM torus T_j is reconstructed. To that end, N points $\boldsymbol{l}_n$ (the number of points $N \in [100, 200]$ depending on the slenderness of the KAM torus to reconstruct) are distributed along the associated closed streamline L_j, and N Poincaré planes are defined by the planes orthogonal to L_j in the points $\boldsymbol{l}_n$. Poincaré sections of the quasiperiodic streamline demarcating T_j are then computed on each of these Poincaré planes perpendicular to L_j. The contour of the KAM torus on each Poincaré plane is then obtained by a cubic spline interpolation. Finally, all N contours are interpolated by cubic Hermitian splines to define the contiguous KAM torus targeted.

C. Evolution of KAM tori for increasing Reynolds number

1. Cubic cavity with $(\Gamma, \Lambda) = (1, 1)$

For the cubic cavity with $\mathrm{Re} \leq 4$, chaotic streamlines occupy only a minor part of the flow domain. The chaotic region extends along the heteroclinic connection between s_1 and s_2 and along all cavity walls. In the regular region, we only find a single central closed streamline L_1 (not shown). For $\mathrm{Re} > 4$, the connection between s_1 and s_2 breaks, and no resonance phenomena are observed for $\mathrm{Re} \leq 10$.

At $\mathrm{Re} = 100$, the chaotic and regular regions occupy approximately one half of the domain each (Fig. 9). A massive set of nested KAM tori is found around the central closed streamline L_1 [diamond in Fig. 9(a)]. As described in Sec. IV B 1, at a resonance, a KAM torus breaks up, giving way to an elliptic closed streamline and a complementary hyperbolic closed streamline. Such resonances must have occurred between $\mathrm{Re} = 10$ and $\mathrm{Re} = 100$. The elliptic closed streamlines generated through these resonances show up as fixed points with periods 7 (L_7, 7:1 resonance) and 6 (L_6, 6:1 resonance) in the Poincaré section on $x = 1/2$ shown in Fig. 9(a). Again, each resonance and torus breakdown is a consequence of the Poincaré–Birkhoff theorem, and a chaotic layer forms around the newly created torus surrounding the resonant elliptic streamline.

The two layers of chaotic streamlines that develop about the closed hyperbolic streamlines are clearly recognized in Fig. 9(a). The chaotic layer about the 7:1 resonance is separated from the exterior chaotic sea by a layer of regular streamlines contained between the regular KAM surfaces S_B and S_C. To make sure that the tori S_A, S_B, and S_C are transport barriers for the flow (Oteski *et al.*, 2014), we considered their turnover and winding periods. A quasiperiodic streamline on any of these tori integrated for at least 12 times the ratio between the longest and the shorted characteristic period. Since the streamlines remained on a torus, they represent transport barriers. This same criterion is also used for the other outermost regular surfaces. Another, much thinner, layer of regular streamlines between the 7:1 and the 6:1 resonance exists of which one KAM surface S_A is shown in the figure. These regular layers are made from nested toroidal surfaces and provide transport barriers to chaotic streamlines. The KAM torus S_B (and also S_C) appears as a single closed curve in Fig. 9(a) because the Poincaré section taken at $x = 0.5$ does not cut through the torus hole. This is quantified considering that the centerline of the torus is approximately given by the stable manifold of s_2, departing from $x = 0.6167$ (Table I).

Figure 9(b) shows the three-dimensional reconstruction of the largest detectable KAM torus T_1 (light gray, the largest torus that does not contain any separated chaotic region) as well as S_A (dark gray) and the closed streamlines L_6 and L_7. Similar three-dimensional views are provided in Figs. 10(b) and 11(b) for higher Reynolds numbers.

Upon an increase of the Reynolds number to $\mathrm{Re} = 200$, the main KAM torus T_1 has shrunk considerably, and the transport barriers provided by S_A and $S_{B,C}$ have vanished (Fig. 10). From the Poincaré section at $x = 0.5$ for $\mathrm{Re} = 200$ shown in Fig. 10(a), we find a 7:1 resonance, now located in the chaotic sea. The corresponding set of slender KAM tori denoted T_7 winds seven times about T_1. Further away from the central regular region, we find a regular structure T_4 with period four, which itself is surrounded by another set of KAM tori T_{12} with period 12. We expect that two successive resonances have taken place at intermediate Reynolds numbers $100 < \mathrm{Re}_1 < \mathrm{Re}_2 < 200$ such that at a first resonance, T_4 is created at $\mathrm{Re}_1 \in (100, 200)$, followed by a second resonance within T_4, leading to the KAM tori T_{12} at $\mathrm{Re}_2 \in (\mathrm{Re}_1, 200]$. This explains the KAM torus T_4 winding four times about T_1 and being surrounded by T_{12}, which appears in the Poincaré section as threefold regular islands about T_4.

Further increasing the Reynolds number to $\mathrm{Re} = 300$ (Fig. 11), the volume occupied by regular streamlines has become even smaller. However, the structure with a main regular region T_1 around which regular islands are arranged is preserved. We find a 5:1 resonance with KAM tori T_5 outside of the main KAM torus T_1. A secondary 4:1 resonance arises around T_5, leading to T_{20} and forming regular islands in the Poincaré plane. The corresponding closed streamline L_{20} closes after winding 20 times about the main KAM torus T_1. Similar to what was observed at $\mathrm{Re} = 100$, a 7:1 resonance occurs for $\mathrm{Re} = 300$ inside the main system of KAM tori, giving rise to the KAM tori T_7 and creating a thin chaotic layer sealed from the chaotic sea by KAM tori between S_A and S_B [cf. zoom in Fig. 11(a)].

For $\mathrm{Re} = 400$ (not shown), regular regions are not observed anymore for the cubic cavity. This is consistent with the results of Ishii *et al.* (2012) who did not find any regular regions for $\mathrm{Re} > 335$ in cubic cavities.

2. Shallow cavity with $(\Gamma, \Lambda) = (0.4, 1)$

The flow topology for a shallow cavity with $(\Gamma, \Lambda) = (0.4, 1)$ for $\mathrm{Re} = 100$, 200, 300, and 400 evolves in a similar way as for the cubic cavity with $(\Gamma, \Lambda) = (1, 1)$. Poincaré sections and at $x = 3/4$ three-dimensional views of KAM tori are shown in Figs. 12–15. A series of transport barriers and resonance phenomena is observed for $(\Gamma, \Lambda) = (0.4, 1)$, as well.

For $\mathrm{Re} = 100$, more and higher resonances are found in the shallow cavity as compared to the cubic cavity. Apart from T_1, we could identify the higher-order KAM sets T_{12}, T_{15}, T_{19}, T_{20}, T_{22}, and

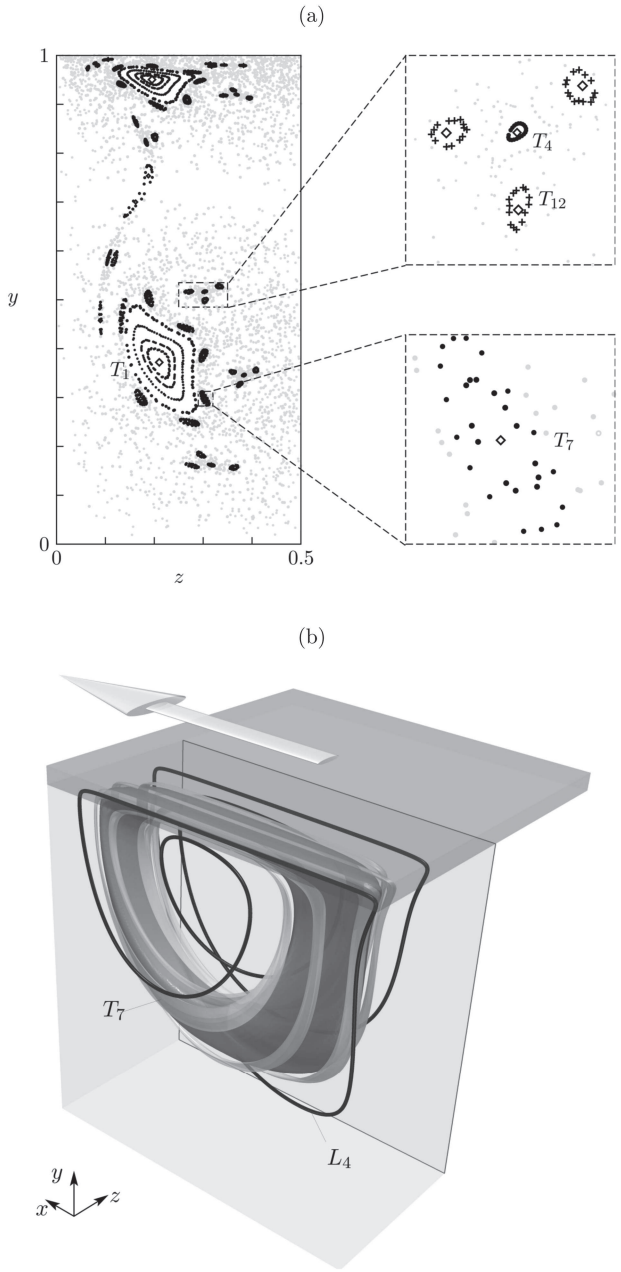

FIG. 10. (a) Poincaré section on $x = 1/2$ for $\mathrm{Re} = 200$, $\Gamma = 1$, and $\Lambda = 1$. Gray dots, black dots, and diamonds indicate chaotic, regular, and closed streamlines, respectively. (b) Three-dimensional reconstruction of the outermost surface of the 7-periodic KAM torus (light gray), 4-periodic closed streamline L_4, and the outermost surface of the main KAM torus T_1 (dark gray).

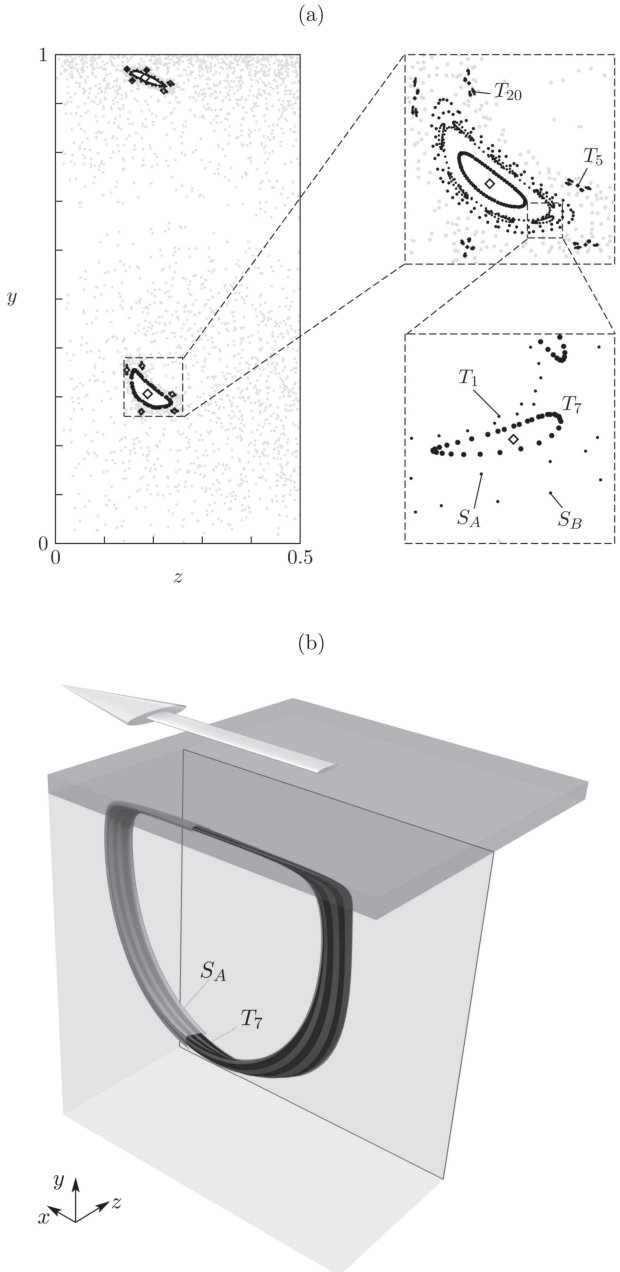

FIG. 11. (a) Poincaré section on $x = 1/2$ for $\mathrm{Re} = 300$, $\Gamma = 1$, and $\Lambda = 1$. Gray dots, black dots, and diamonds indicate chaotic, regular, and closed streamlines, respectively. (b) Three-dimensional reconstruction of the transport barrier S_A (light gray), the outermost surface of the 7-periodic KAM torus T_7 (black), and the outermost surface of the main KAM torus T_1 (dark gray).

T_{25}. The order grows with the distance from the closed streamline L_1. The innermost resonance T_{12} is separated from the other high-order KAM structures by a thin set of period-one KAM tubes of which S_A is indicated in Fig. 12(a).

For $\mathrm{Re} = 200$, the KAM tori generated from high-order resonances have disappeared (Fig. 13). However, transport barriers sealing chaotic layers still exist. Four mutually sealed chaotic regions are identified in each half of the cavity: the chaotic layer between the

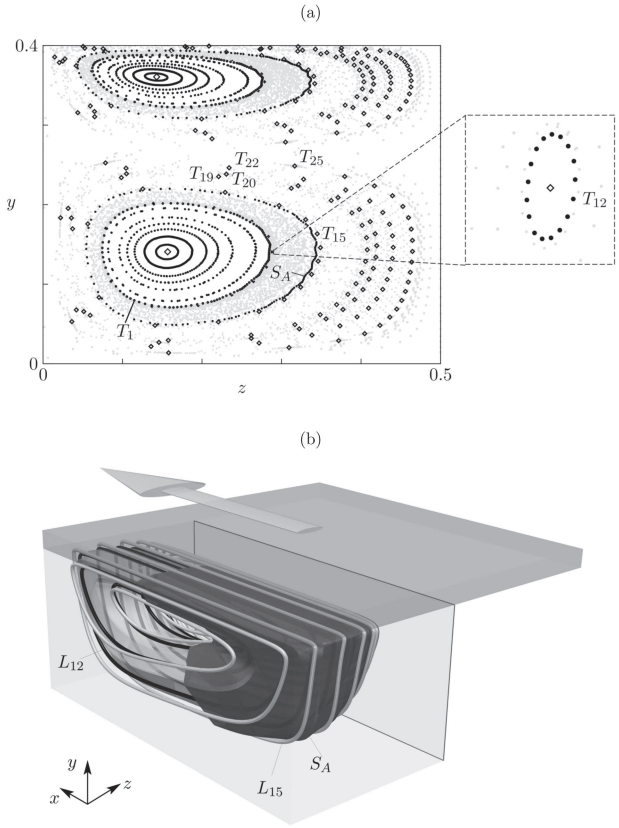

FIG. 12. (a) Poincaré section on $x = 3/4$ for Re = 100, $\Gamma = 0.4$, and $\Lambda = 1$. Gray dots, black dots, and diamonds indicate chaotic, regular, and closed streamlines, respectively. (b) Three-dimensional reconstruction of the transport barrier S_A (dark gray), 12- and 15-periodic closed streamlines L_{12} and L_{15}, respectively, and the outermost surface of the main KAM torus T_1 (light gray).

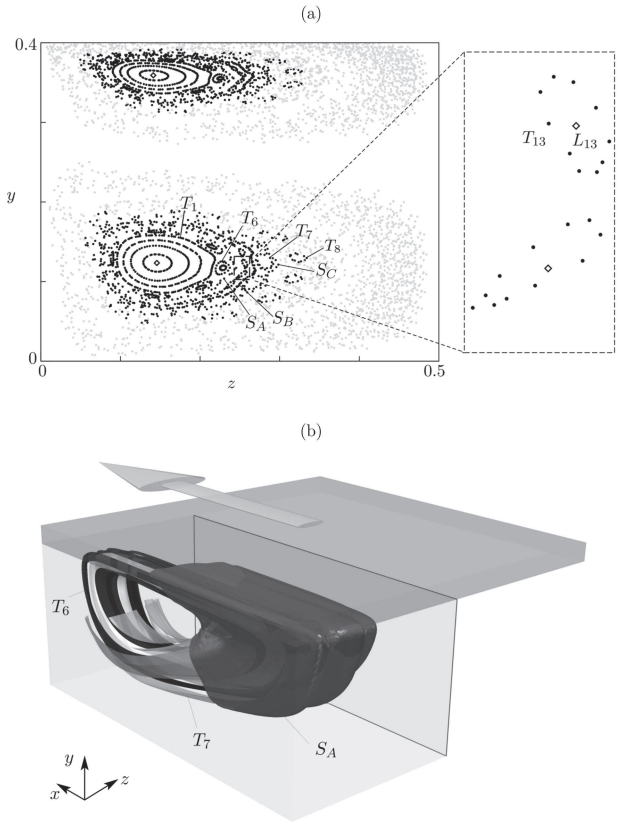

FIG. 13. (a) Poincaré section on $x = 3/4$ for Re = 200, $\Gamma = 0.4$, and $\Lambda = 1$. Gray dots, black dots, and diamonds indicate chaotic, regular, and closed streamlines, respectively. (b) Three-dimensional reconstruction of the transport barrier S_A (dark gray), the outermost surface of the 6- and 7-periodic KAM tori T_6 and T_7, respectively, and the outermost surface of the main KAM torus T_1 (light gray).

core structure T_1 and the transport barrier S_A, the one between S_A and S_B, the chaotic layer between S_B and S_C, and the outer chaotic sea between S_C and the cavity walls [Fig. 13(a)].

Upon a further increase of the Reynolds number (Fig. 14 for Re = 300), regular-flow barriers could no longer be identified. However, as explained by Ishii *et al.* (2012), several primary resonances can be found for Re = 300 [Fig. 14(a)] and for Re = 400 [Fig. 15(a)]. Some of these also exhibit secondary resonances. For Re = 300, e.g., T_{25} winds five times about T_5. Moreover, for Re = 400, the 3:1 resonance, which arises very close to L_1, is surrounded by a transport barrier (S_A in Fig. 15).

3. Long cavity with $(\Gamma, \Lambda) = (1, 2)$

Poincaré sections at $x = 1/2$ and three-dimensional views of the main topological elements for $(\Gamma, \Lambda) = (1, 2)$ and Re = 100, 200, 300, and 400 are shown in Figs. 16–19. For the lowest Reynolds number, Re = 100 (Fig. 16), the flow topology is similar to the one for Re = 200 in the shallow cavity. For Re = 200 and 300 (Figs. 17 and 18), however, KAM tori with high periods are absent, and the KAM torus T_1 remains the only regular region in the flow. Upon increasing Re, T_1 shrinks without any further resonance, and the closed streamline L_1, located at $z \approx 0.2$ for Re = 300, moves closer to the end wall at $z = 0$. Similar scenarios without further resonances have been reported for a two-sided lid-driven cavity (Romanò *et al.*, 2017) and a partially filled rotating drum (Romanò *et al.*, 2017).

As the Reynolds number is increased to Re = 400 (Fig. 19), T_1 has vanished completely. However, a new set of period-one KAM tori (and its mirror-symmetric counterpart) is born very close to the midplane $z = 1$ and, therefore, denoted T_{1M}. The new set of KAM tori is related to a change of the streamline topology in the midplane shown in Fig. 6.

The two-dimensional unstable manifolds of V_1 and a stable two-dimensional manifold of V_2 approach each other closely in the bulk and closely embrace the separated flow region defined by the KAM tori shown in Fig. 19(a). As V_2 is not connected with the bottom wall, also, the KAM tori T_{1M} are not in contact with the bottom wall. Since the streamlines on the midplane spiral very densely, the

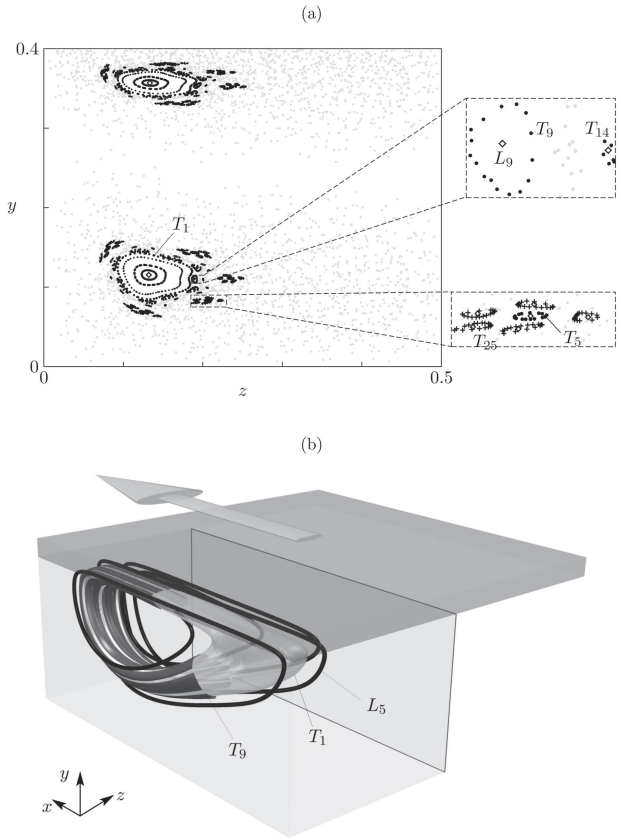

FIG. 14. (a) Poincaré section on $x = 3/4$ for $\mathrm{Re} = 300$, $\Gamma = 0.4$, and $\Lambda = 1$. Gray dots, black dots, and diamonds indicate chaotic, regular, and closed streamlines, respectively. (b) Three-dimensional reconstruction of the outermost surface of the 9-periodic KAM torus T_9 (dark gray), the 5-periodic closed streamline L_5, and the outermost surface of the main KAM torus T_1 (light gray).

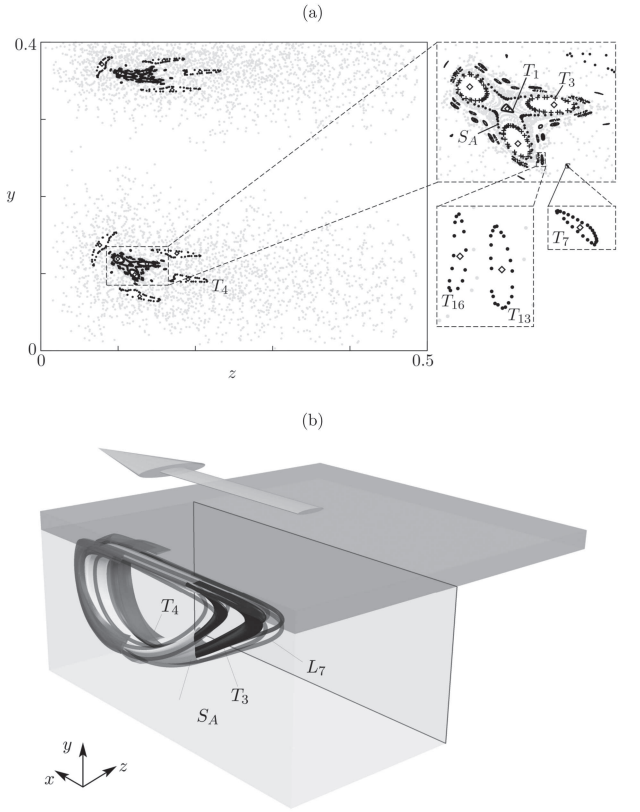

FIG. 15. (a) Poincaré section on $x = 3/4$ for $\mathrm{Re} = 400$, $\Gamma = 0.4$, and $\Lambda = 1$. Gray dots, black dots, and diamonds indicate chaotic, regular, and closed streamlines, respectively. (b) Three-dimensional reconstruction of the transport barrier S_A, the outermost surface of the 3- and 4-periodic KAM tori T_3 and T_4, respectively, and the 7-periodic closed streamline L_7.

streamlines on the two-dimensional manifolds of V_1 and V_2 leaving the midplane advance very slowly, as does the winding on the KAM tori T_{1M}. Related to this is the very small component of the velocity w near the midplane (see Fig. 7).

Associated with the flow reversal near the midplane and the upstream corner, the inflow motion near s_6 [cf. Fig. 4(a)] has changed into an outflow motion (see Fig. 6), and the fluid that is transported to the midplane near the upstream corner must escape along the upstream wall and along the moving lid to arrive at the downstream corner (see Fig. 8) where it is fed back to the midplane-departing stream. The change of the direction of w near the upstream corner in which the corner eddy is located leads to the creation of the free spiraling-in saddle focus s_8, indicated by a dot in Fig. 7.

Similar separated KAM tori have been found by Ishii and Adachi (2010) for the same Reynolds number and $\Gamma = 1$, but for $\Lambda = 6.55$. On increasing the Reynolds number for $(\Gamma, \Lambda) = (1, 6.55)$, Ishii and Adachi (2006) even found multiple separated regions in the plane $x = 0.5$ with KAM tori very close to the bottom of the cavity and which do not always extend up to the midplane. The creation of the separated region (or regions) near the symmetry plane at $z = \Lambda/2$ is a fundamental topological change. However, it does not hamper the chaotic mixing process described in Sec. IV A (Fig. 5). Merely, the separated region is by-passed by the fluid passing s_2 and being transported to near s_1 on the end walls. The spontaneous separation resembles the phenomenon of vortex breakdown in cylinders with a rotating bottom and a flat free (symmetry) surface, where the separation bubble extends up to the free surface (symmetry plane) (Spohn *et al.*, 1993). The vortex breakdown in contact with the symmetry plane typically arises in the region in which the flow departs from the symmetry plane (Jacono *et al.*, 2009). In the present cavity flow, this is the region near the walls.

V. INFINITELY EXTENDED CAVITIES

The flow topology in cuboidal cavities is significantly affected by the no-slip end walls at $z = 0, \Lambda$. Therefore, it is of interest to inquire the cavity flow in which the end-wall effects do not

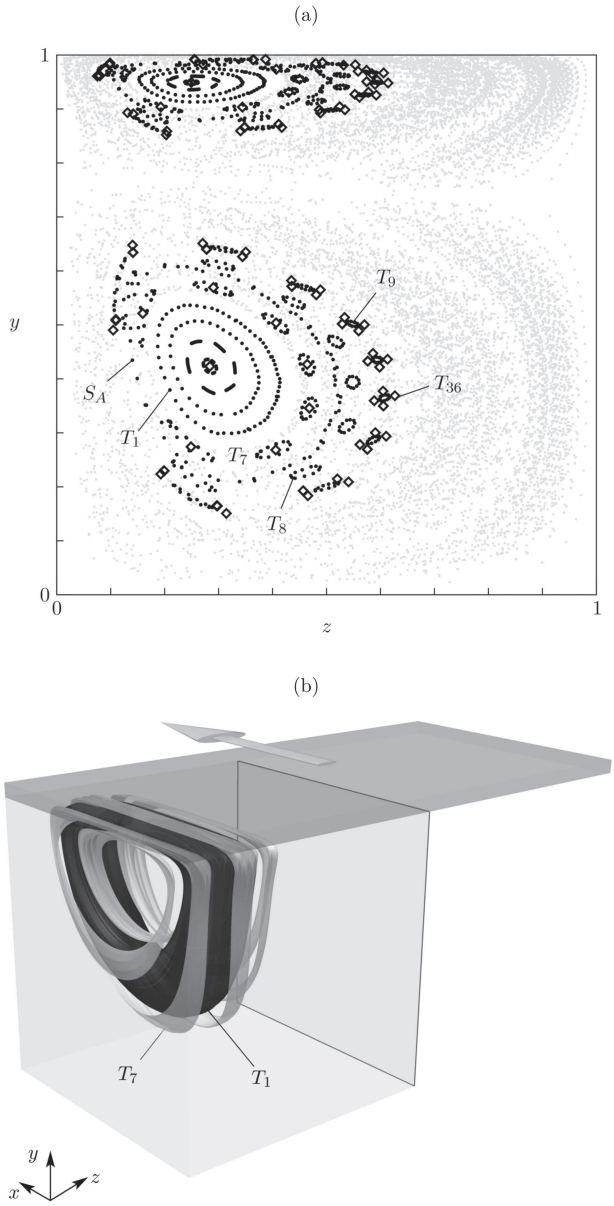

FIG. 16. (a) Poincaré section on $x = 1/2$ for $\mathrm{Re} = 100$, $\Gamma = 1$, and $\Lambda = 2$. Gray dots, black dots, and diamonds indicate chaotic, regular, and closed streamlines, respectively. (b) Three-dimensional reconstruction of the main KAM torus T_1 (dark gray) and of the outermost surface of the 7-periodic KAM torus T_7 (light gray).

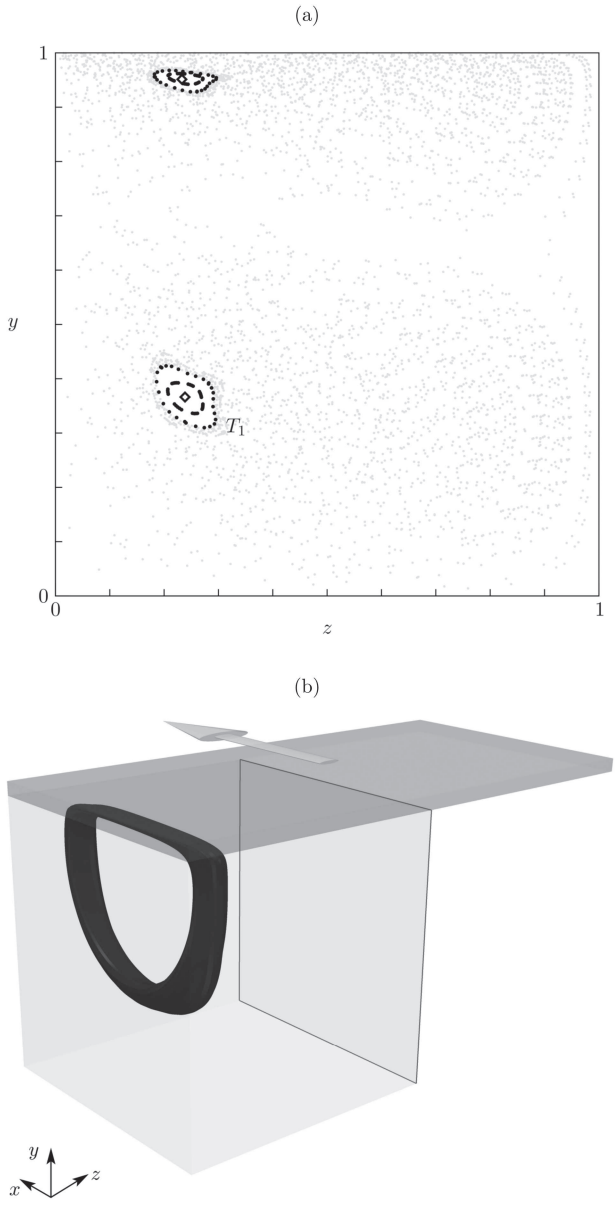

FIG. 17. (a) Poincaré section on $x = 1/2$ for $\mathrm{Re} = 200$, $\Gamma = 1$, and $\Lambda = 2$. Grey dots, black dots, and diamonds indicate chaotic, regular, and closed streamlines, respectively. (b) Three-dimensional reconstruction of the KAM torus T_1.

play a role. To this end, we consider an infinitely extended cavity ($\Lambda \to \infty$). The basic flow $\boldsymbol{u}_0(x, y)$ is steady and independent of the z coordinate and corresponds to the classical two-dimensional cavity flow. At a critical Reynolds number Re_c, the translational symmetry is spontaneously broken, and a three-dimensional perturbation flow $\boldsymbol{u}_{\mathrm{TG}}$ bifurcates from the basic flow owing to a centrifugal instability within the aspect ratio range $\Gamma \in [0.888, 1.163]$ with the total flow being $\boldsymbol{u} = \boldsymbol{u}_0 + \boldsymbol{u}_{\mathrm{TG}}$. According to Albensoeder *et al.* (2001b), the bifurcation is supercritical, and the finite-amplitude three-dimensional flow $\boldsymbol{u}_{\mathrm{TG}}$ arises as Taylor–Görtler vortices on the walls in the curved boundary layer of the basic flow if the critical Reynolds number is exceeded. Here, we consider the supercritical three-dimensional flow for $\Gamma = 1$. The Taylor–Görtler vortices $\boldsymbol{u}_{\mathrm{TG}}$ are steady and three-dimensional. Figure 20(a) shows one period in

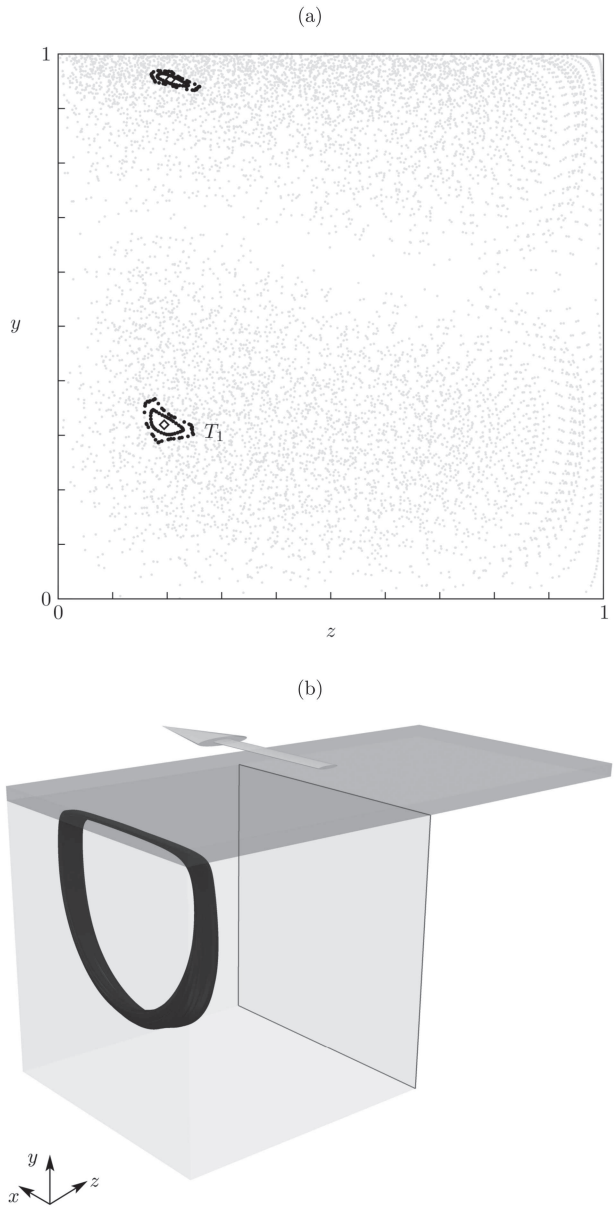

FIG. 18. (a) Poincaré section on $x = 1/2$ for Re $= 300$, $\Gamma = 1$, and $\Lambda = 2$. Gray dots, black dots, and diamonds indicate chaotic, regular, and closed streamlines, respectively. (b) Three-dimensional reconstruction of the KAM torus T_1.

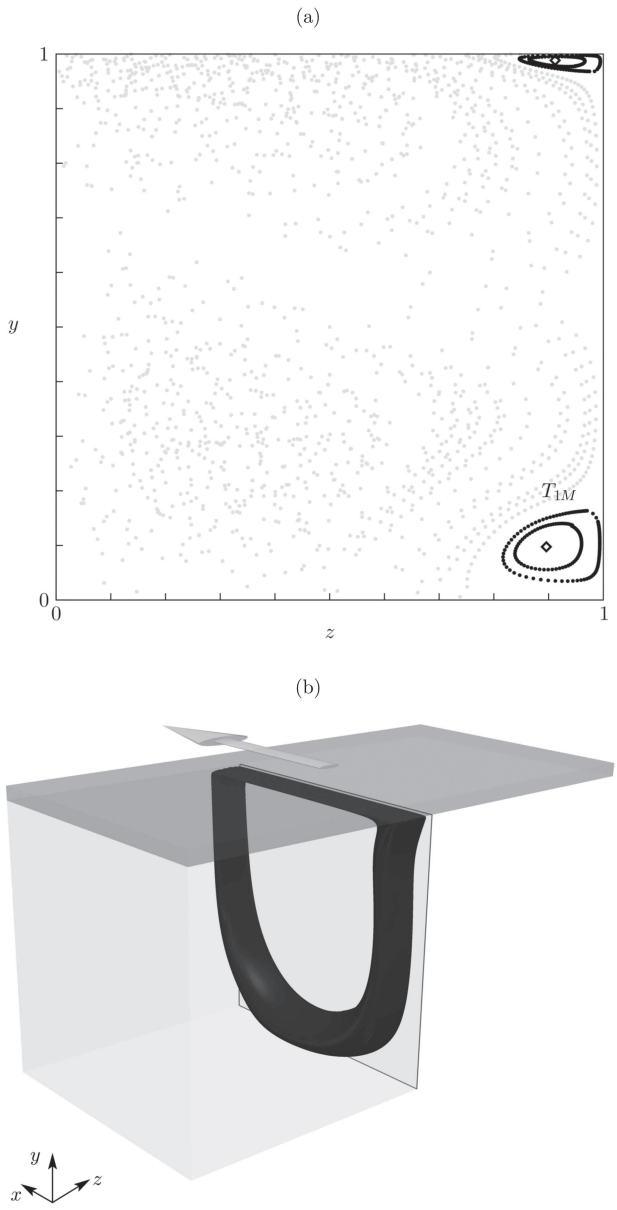

FIG. 19. (a) Poincaré section on $x = 1/2$ for Re $= 400$, $\Gamma = 1$, and $\Lambda = 2$. Gray dots, black dots, and diamonds indicate chaotic, regular, and closed streamlines, respectively. (b) Three-dimensional reconstruction of the KAM torus T_{1M} located near the mirror-symmetry plane.

z of the critical mode $\boldsymbol{u}_{\mathrm{TG}}^{(c)}$ in the plane $y = 0.5$, which is superimposed on the basic flow. One period λ in z comprises two counter-rotating Taylor–Görtler vortices (two cells). Note the symmetry planes (left–right symmetry of the flow pattern). The Taylor vortices are clearly seen above the sidewall upstream of the moving wall [the bottom of Fig. 20(a)]. On the sidewall downstream from the moving wall [top of Fig. 20(a)], the sense of rotation of the vortices has changed. This can also be inferred from the iso-surfaces of the spanwise velocity $w = w_{\mathrm{TG}}$ of the periodic flow at Re $= 900$, which are shown in Fig. 20(b) over three periods. From Fig. 20(b), one can recognize that the vortices extend from the bottom of the cavity over the upstream sidewall to the moving lid.

For Re $>$ Re$_c$, the wavelength of the Taylor–Görtler vortices is not uniquely determined and can range in a certain band of

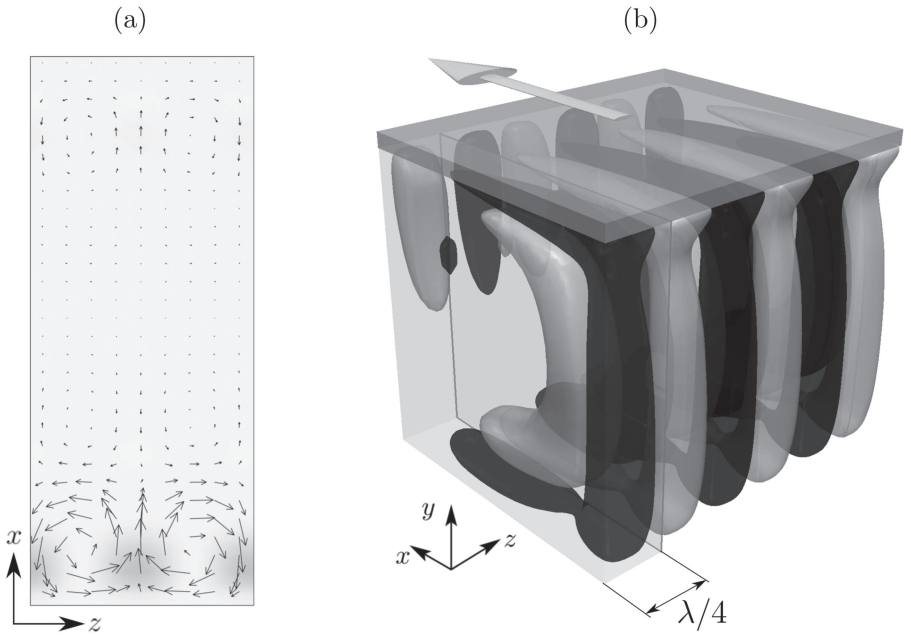

FIG. 20. (a) Structure of one pair of Taylor–Görtler vortices ($\boldsymbol{u}_{\mathrm{TG}}^{(c)}$, two cells) at the critical onset for $\Gamma = 1$ and $\mathrm{Re} = \mathrm{Re}_c = 783.9$ shown in the plane $y = 0.5$ (reproduced from Albensoeder *et al.*, 2001b). The lid moves from the bottom to the top parallel to the plane shown. (b) Isosurfaces of the velocity component w of the total flow over three periods at $\mathrm{Re} = 900$. Since $w_0 = 0$, the isosurfaces shown are identical to the isosurfaces w_{TG} of the finite-amplitude Taylor–Görtler vortices.

wave numbers. As the wavelength at the critical point $\lambda = \lambda_c(\Gamma = 1) = 2\pi/k_c(\Gamma = 1) = 0.406\,78$ is well in the range for which periodic Taylor–Görtler vortices exist (Albensoeder and Kuhlmann, 2006), we keep the spanwise period $\lambda = \lambda_c$ constant. Since the time-dependent flow sets in only for $\mathrm{Re} > 900$ (Albensoeder and Kuhlmann, 2006), periodic boundary conditions are used to compute steady flows for Reynolds numbers ranging from $\mathrm{Re} = 800 \approx 1.02 \times \mathrm{Re}_c$ (sightly supercritical) over $\mathrm{Re} = 850$ to $\mathrm{Re} = 900 \approx 1.15 \times \mathrm{Re}_c$.

A. Symmetries and fixed points

Each individual Taylor–Görtler vortex is bounded by symmetry planes at constant values of z, a width $\lambda/2$ apart [cf. Figs. 20 and 21(a)]. Let us define the origin of the coordinate system such that these mirror-symmetry planes (cell boundaries) are located at $z_n = (2n-1)\lambda/4$, $n \in \mathbb{Z}$. Then, the Taylor–Görtler flow (as well as the full three-dimensional flow) satisfies

$$u_{\mathrm{TG}}(z - z_n) = u_{\mathrm{TG}}(z_n - z), \tag{6a}$$

$$v_{\mathrm{TG}}(z - z_n) = v_{\mathrm{TG}}(z_n - z), \tag{6b}$$

$$w_{\mathrm{TG}}(z - z_n) = -w_{\mathrm{TG}}(z_n - z). \tag{6c}$$

These symmetry planes are preserved for higher Reynolds numbers until the onset of time-dependence. Therefore, we only need to consider a single representative Taylor–Görtler cell confined to $z \in [z_0, z_1] = [-\lambda/4, \lambda/4]$. Due to its sinusoidal dependence on z, the critical normal mode $\boldsymbol{u}_{\mathrm{TG}}^{(c)}$ at the onset of a three-dimensional flow exhibits the additional symmetry with respect to the vortex center plane at $z = 0$ (not the full flow $\boldsymbol{u}$),

$$u_{\mathrm{TG}}^{(c)}(z) = -u_{\mathrm{TG}}^{(c)}(z), \tag{7a}$$

$$v_{\mathrm{TG}}^{(c)}(z) = -v_{\mathrm{TG}}^{(c)}(z), \tag{7b}$$

$$w_{\mathrm{TG}}^{(c)}(z) = w_{\mathrm{TG}}^{(c)}(z). \tag{7c}$$

In the total flow field $\boldsymbol{u}$, similar as for the cuboidal cavity flow, there exist two saddle foci s_1 (spiraling-in at $z = -\lambda/4$) and s_2 (spiraling-out at $z = \lambda/4$) on the two symmetry planes bounding the Taylor–Görtler cell under consideration. However, in the present case of a periodic cellular flow, both saddle foci are non-degenerate. Different from the cuboidal cavity flow, there also exist two non-degenerate saddle limit cycles on each plane $z = \pm\lambda/4$ ($W_{1,3}$ on $z = -\lambda/4$ and $W_{2,4}$ on $z = \lambda/4$). These two saddle limit cycles arise due to the fine structure of the Taylor–Görtler cell in the (x, y) plane. The Taylor–Görtler vortices $\boldsymbol{u}_{\mathrm{TG}}$ scale with the thickness of the curved boundary layers on the solid walls and thus have a very small width of $\lambda/2$ in the spanwise direction z and also a corresponding small height [e.g., in the x direction in Fig. 20(a)]. Therefore, they are not space filling, and each toroidal Taylor–Görtler vortex drives a similar, but much weaker, counter-rotating vortex on its radially inward side. The weak counter-rotating inner vortices can be seen in Fig. 20(a) just above the bottom pair of Taylor–Görtler vortices. We call these weak counter-rotating vortices *secondary Taylor–Görtler vortices*. The boundary between the primary and the secondary vortices manifests itself by the saddle limit cycles W_3 and W_4 on the cell boundaries of the total flow $\boldsymbol{u}$ [Fig. 21(b)]. Similarly, the counter-rotating secondary Taylor–Görtler vortices induce counter-rotating tertiary Taylor–Görtler vortices on their inner sides, co-rotating with the primary Taylor–Görtler vortices [not visible on the velocity scale in Fig. 20(a)], which lead to the saddle-limit cycles W_1 and W_2.

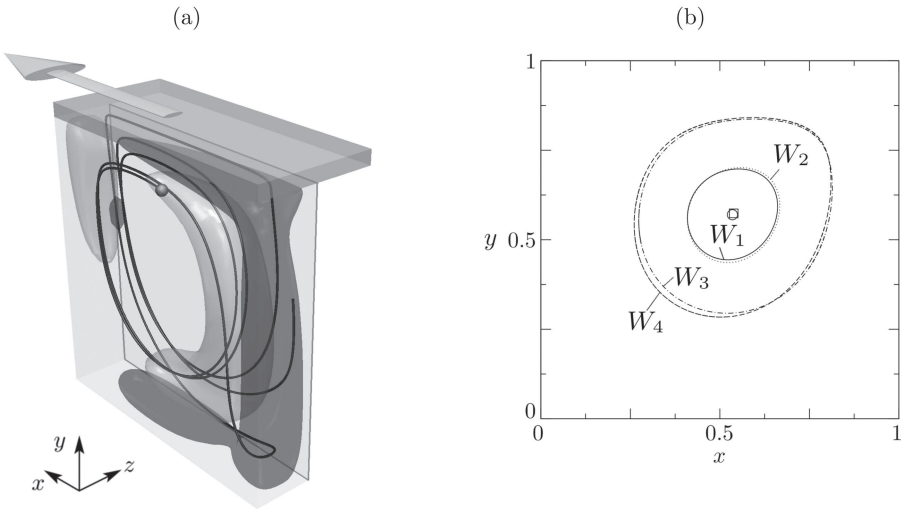

FIG. 21. Isosurfaces of the spanwise velocity for $w = 0.01$ (light gray) and $w = -0.01$ (dark gray) shown within half a wavelength $z \in [-\lambda/4, \lambda/4]$ for Re = 900, $\Gamma = 1$, and $\lambda = \lambda_c = 0.406\,78$. A typical streamline initialized in the primary Taylor–Görtler vortex (dot) is depicted in dark gray. (b) Projections of the free saddle focus s_1 (circle) and saddle limit cycles W_1 (solid line) and W_3 (dashed–dotted line) on the mirror-symmetry plane $z = -\lambda/4$ and those on $z = +\lambda/4$ [s_2 (square), W_2 (dotted line), W_4 (dashed line)] for $\Gamma = 1$, $\lambda = \lambda_c = 0.406\,78$, and Re = 800.

At the critical point $\mathrm{Re} = \mathrm{Re}_c$, the projections onto the (x, y) plane of the saddle foci and the saddle limit on $z = +\lambda/4$ are identical to those on $z = -\lambda/4$ due to the anti-symmetry (7) of the critical mode $\boldsymbol{u}_{\mathrm{TG}}^{(c)}$ (a single Fourier mode). For $\mathrm{Re} > \mathrm{Re}_c$, however, the nonlinear interaction generates higher harmonics (see, e.g., Davey, 1962). These higher harmonics break the antisymmetry (7) with respect to $z = 0$ of $\boldsymbol{u}_{\mathrm{TG}}$. As a result, the saddle limit cycles of the full flow $\boldsymbol{u}$ on the cell boundaries differ. Accurate locations of the non-degenerate limit cycles of $\boldsymbol{u}$ are shown in Fig. 21(b) for Re = 800.

The heteroclinic connection between the two saddle foci and the four saddle limit cycles is delicate (Table VI). The connectedness is topologically important because two-dimensional heteroclinic manifolds represent transport barriers to the three-dimensional flow. We find the saddle limit cycles s_1 and s_2 being heteroclinically connected for Re = 800 and 850 and becoming disconnected for Re = 900. On the other hand, the saddle limit cycles W_1–W_2 and W_3–W_4 are always disconnected, except for $\mathrm{Re} = \mathrm{Re}_c$, but the connection is only very slightly perturbed for Re = 850 and Re = 900. To indicate the evident quantitative difference between a broken connection that extends deeply into the periodic cell (for Re = 800) and a localized broken connection that emerges in the strict proximity of the attracting/repelling critical object (for Re = 850 and Re = 900), we shall use, in the following, the terminologies *slightly broken heteroclinic connection* and *slightly disconnected critical objects*. We use the term *slightly broken* for a broken heteroclinic connection for which the unstable (stable) manifold still approaches the stable (unstable) critical object to a distance less than 0.01 upon the first approach. The slightly broken connections and the intersection of the respective two-dimensional manifolds are a source of chaotic advection in the system. A sketch of the intact and slightly broken heteroclinic connections is reported in Fig. 22.

The streamline topology in the mirror-symmetry planes for Re = 900 is presented in Fig. 23(a) for $z = -\lambda/4$ and in Fig. 23(b) for $z = \lambda/4$. Streamlines are only shown for the regions outside the outermost limit cycles W_3 and W_4 because the spiraling-in and the spiraling-out motions inside W_3 and W_4, respectively, result in very dense streamlines that are difficult to distinguish at the scale of the figures. The streamline topologies on the symmetry planes are very similar to the one on the symmetry plane in the cubic cavity [Fig. 4(a)]: In both cases, we find a free saddle focus near the downstream corner of the cavity and a set of half-saddle points for both corners. For the Taylor–Görtler flow shown, the saddle focus s_8 is detached from the bottom wall [gray dot in Fig. 23(b)]. This was also found for $\mathrm{Re} \approx 1$ in cuboidal cavity flows (not shown). Details of the streamline structure near the bottom corners are depicted in Figs. 4(c) and 4(d) for $z = -\lambda/4$ and $z = \lambda/4$, respectively. The major distinction from cuboidal cavities is the presence of the saddle limit cycles $W_{1,2,3,4}$ in the periodic flow.

The properties of the spiraling-in (s_1) and the spiraling-out (s_2) saddle foci are given in Tables VII and VIII, in which the location of the two fixed points and the eigenvalues and eigenvectors of the velocity-gradient tensors evaluated at s_1 and s_2 are specified.

TABLE VI. Relation between saddle foci and saddle limit cycles in a periodic Taylor–Görtler flow for $\lambda = 0.406\,78$.

Re	Re_c	800	850	900
$s_1 \to s_2$	Connected	Connected	Connected	Disconnected
$W_1 \to W_2$	Connected	Disconnected	Slightly disconnected	Slightly disconnected
$W_3 \to W_4$	Connected	Disconnected	Slightly disconnected	Slightly disconnected

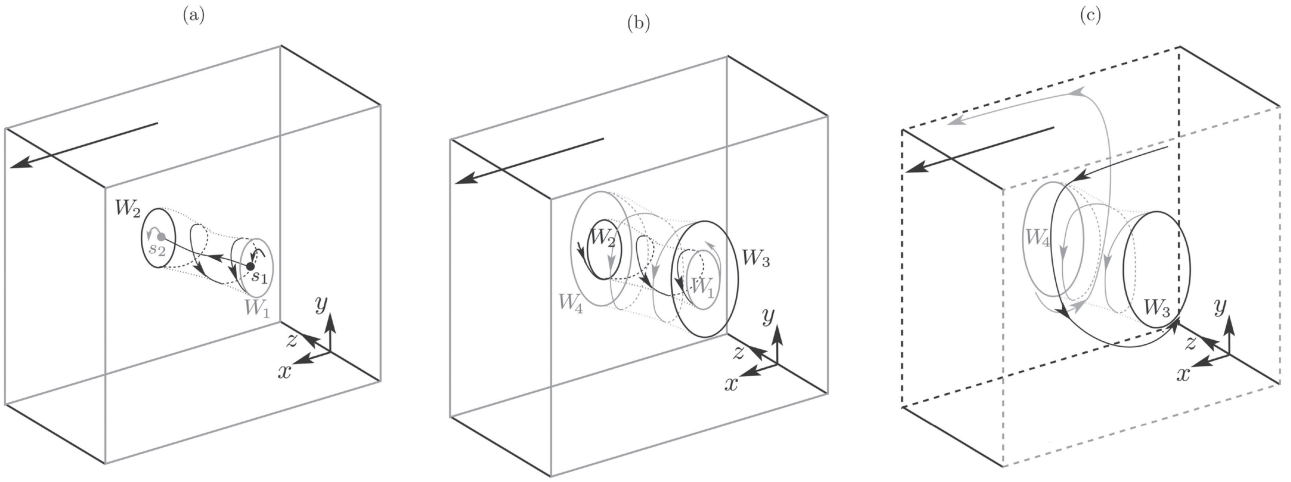

FIG. 22. Transport within a Taylor–Görtler cell between $z = -\lambda/4$ and $z = \lambda/4$. Although the sketch shows heteroclinic connections, the critical objects on the symmetry planes are numerically slightly disconnected between s_1 and s_2, W_1 and W_2, and W_3 and W_4. The motion of fluid elements outside the slightly broken heteroclinic connection between W_3 and W_4 is sketched in (c).

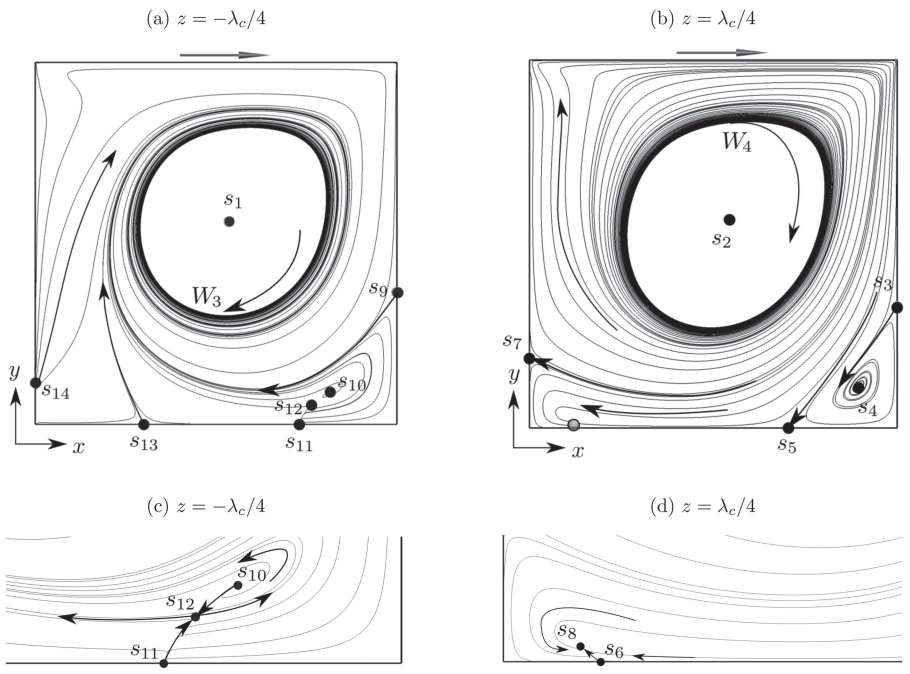

FIG. 23. Streamlines on the mirror-symmetry planes $z = -\lambda_c/4$ (a) and $z = \lambda_c/4$ (b) for Re = 900 and $(\Gamma, \lambda) = (1, \lambda_c)$ (thin lines). The arrows on top indicate the direction of the lid motion. Dots represent the critical points with the gray dot symbolizing two close-by critical points, better seen in (d). The flow direction and stable/unstable manifolds are indicated by bold arrows. Zooms (c) and (d) into the bottom-right and bottom-left corners show streamlines and critical points for $z = -\lambda_c/4$ and $z = \lambda_c/4$, respectively.

TABLE VII. Location of the saddle foci $s_{1,2}$ on $z = \pm\lambda_c/4$ and corresponding eigenvalues of the velocity-gradient tensor.

Re	$\boldsymbol{x}_{s_1}$	$\lambda_{1,2}^{s_1}$	$\lambda_3^{s_1}$	$\boldsymbol{x}_{s_2}$	$\lambda_{1,2}^{s_2}$	$\lambda_3^{s_2}$
800	(0.5350, 0.5699)	-0.003 ± 1.017i	0.006	(0.5386, 0.5737)	0.0006 ± 1.017i	-0.0012
850	(0.5350, 0.5634)	-0.004 ± 0.971i	0.008	(0.5411, 0.5702)	0.0022 ± 0.971i	-0.0044
900	(0.5357, 0.5596)	-0.005 ± 0.937i	0.010	(0.5426, 0.5673)	0.0033 ± 0.937i	-0.0066

TABLE VIII. Normalized eigenvectors of the velocity-gradient tensor at the two saddle foci $s_{1,2}$ on $z = \pm\lambda_c/4$.

Re	$\boldsymbol{v}_{1,2}^{s_1}$	$\boldsymbol{v}_3^{s_1}$
800	$(0.082 \pm 0.699\mathrm{i},\ 0.711,\ 0.000)^{\mathrm{T}}$	$(0.000,\ 0.000,\ 1.000)^{\mathrm{T}}$
850	$(0.083 \pm 0.698\mathrm{i},\ 0.711,\ 0.000)^{\mathrm{T}}$	$(0.000,\ 0.000,\ 1.000)^{\mathrm{T}}$
900	$(0.084 \pm 0.696\mathrm{i},\ 0.713,\ 0.000)^{\mathrm{T}}$	$(0.000,\ 0.000,\ 1.000)^{\mathrm{T}}$
Re	$\boldsymbol{v}_{1,2}^{s_2}$	$\boldsymbol{v}_3^{s_2}$
800	$(0.095 \mp 0.691\mathrm{i},\ 0.716,\ 0.000)^{\mathrm{T}}$	$(0.000,\ 0.000,\ 1.000)^{\mathrm{T}}$
850	$(0.103 \mp 0.684\mathrm{i},\ 0.722,\ 0.000)^{\mathrm{T}}$	$(0.000,\ 0.000,\ 1.000)^{\mathrm{T}}$
900	$(0.106 \mp 0.680\mathrm{i},\ 0.726,\ 0.000)^{\mathrm{T}}$	$(0.000,\ 0.000,\ 1.000)^{\mathrm{T}}$

B. KAM tori and chaotic sea

As the steady two-dimensional flow bifurcates to a steady three-dimensional flow, chaotic streamlines emerge. At the margin of stability, at $\mathrm{Re} = \mathrm{Re}_c$, the critical mode $\boldsymbol{u}_{\mathrm{TG}}^{(c)}$ exists with an infinitesimally small amplitude. Due to the additional symmetry (7) of the critical mode, heteroclinic connections exist at $\mathrm{Re} = \mathrm{Re}_c$ between the two saddle foci $s_{1,2}$ and between the saddle limit cycles $W_{1,2}$ as well as between $W_{3,4}$. For $\mathrm{Re} > \mathrm{Re}_c$, we find most of these connections to be slightly broken (Table VI).

For slightly supercritical driving at $\mathrm{Re} = 800$, the main (outer) Taylor–Görtler vortex is dominated by chaotic streamlines. Only small regular islands are found with KAM systems T_5 and T_6 winding about the main torus T_{1A} (Fig. 24). On the other hand, the flow in the secondary and tertiary (inner) Görtler vortices is found to be partly regular with large sets of KAM tori T_{1B} and T_{1C}, respectively. Up to numerical accuracy, the connection between s_1 and s_2 is preserved at $\mathrm{Re} = 800$. However, W_1 and W_2, as well as W_3 and W_4 are clearly disconnected. This enables the chaotic sea from the main outer Görtler vortex to penetrate the inner cells along the cell boundaries. The gray *lines* in Fig. 24(a) near the connection between s_1 and s_2 (not indicated) must not be mistaken as regular streamlines. This set of densely packed Poincaré returns on the $(x = 1/2)$-plane looking like *lines* is produced by chaotic streamlines, which rapidly wind about the heteroclinic connection between s_1 and s_2 and progress only slowly in the z direction due to the weakness of the tertiary Taylor–Görtler vortex. The presence of higher harmonics in z in the flow field is clearly visible by the asymmetrical placement of the regular regions [black dots in Fig. 24(a)]. A three-dimensional view of the main KAM tori is provided in Fig. 24(b).

Upon an increase of the Reynolds number to $\mathrm{Re} = 850$, the small KAM tori in the primary (outer) Taylor–Görtler vortex vanish completely (Fig. 25). On the other hand, W_1 and W_2, as well as W_3 and W_4 are only slightly disconnected, and the middle and inner Taylor–Görtler vortices become almost regular (T_{1B} and T_{1C}). Therefore, the system T_{1B} and T_{1C} of KAM tori almost seals the outer region from the small inner chaotic sea of the convection cell. The small inner region of chaotic streamlines in the center of the Taylor–Görtler vortex cell exists around the heteroclinic connection between s_1 and s_2. This behavior shows that the size of the KAM tori must not necessarily shrink on an increase of the driving force (Re). Finally, for $\mathrm{Re} = 900$ (Fig. 26), the connection between the two sets of saddle limit cycles is slightly broken, as well as the connection between the two saddle foci. The inner set of KAM tori T_{1C} has shrunk again, while T_{1B} remains nearly $\lambda/2$-filling. Three-dimensional views of the largest reconstructible KAM tori T_{1B} and T_{1C} are shown in Figs. 25(b) and 26(b) for $\mathrm{Re} = 850$ and 900, respectively.

At $\mathrm{Re} \gtrsim \mathrm{Re}_c$, the saddle foci s_1 and s_2 together with the saddle limit cycles W_1 and W_2 make a non-degenerate heteroclinic loop. This loop is topologically similar to a recirculation bubble arising

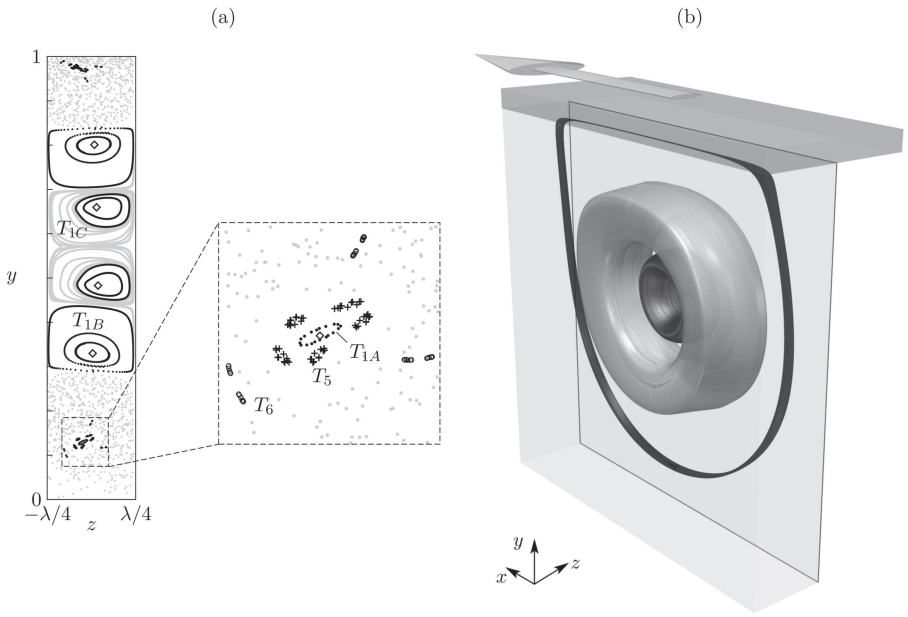

FIG. 24. (a) Poincaré section of fluid element trajectories for $\mathrm{Re} = 800$, $\Gamma = 1$, and $\lambda = \lambda_c$. Gray dots denote chaotic regions, whereas black dots, pluses, and circles refer to regular KAM tori. (b) Three-dimensional reconstruction of the outermost surface of the KAM tori T_{1A}, T_{1B}, and T_{1C}.

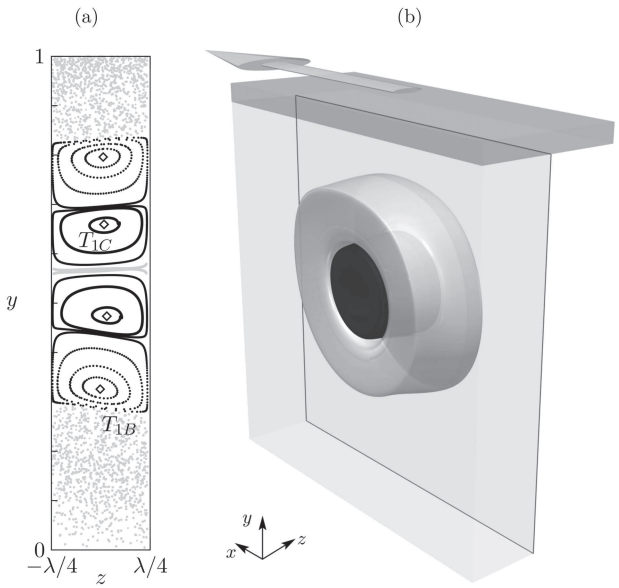

FIG. 25. (a) Poincaré section of fluid element trajectories for Re = 850, $\Gamma = 1$, and $\lambda = \lambda_c$. Gray dots denote chaotic regions, whereas black dots refer to regular KAM tori. (b) Three-dimensional reconstruction of the outermost surface of the KAM tori T_{1B} and T_{1C}.

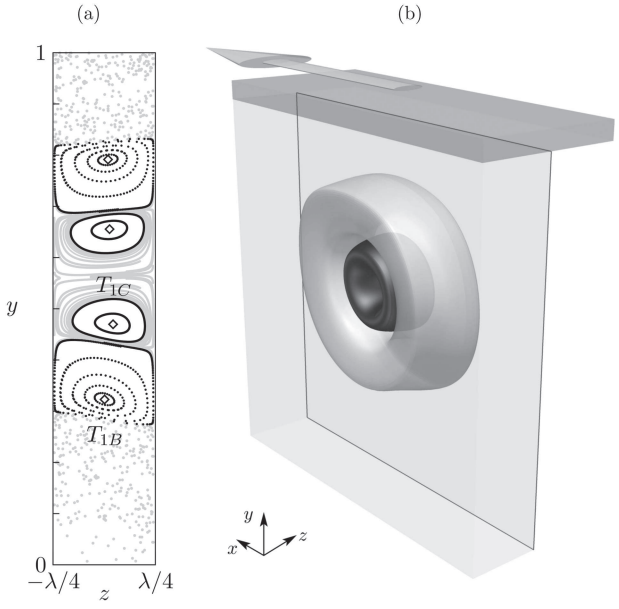

FIG. 26. (a) Poincaré section of fluid element trajectories for Re = 900, $\Gamma = 1$, and $\lambda = \lambda_c$. Gray dots denote chaotic regions, whereas black dots refer to regular KAM tori. (b) Three-dimensional reconstruction of the outermost surface of the KAM tori T_{1B} and T_{1C}.

from axisymmetric vortex breakdown (see Escudier, 1984 or Fig. 5 of Sotiropoulos *et al.*, 2001) or from a perturbed Hill vortex (Kroujiline and Stone, 1999). Owing to the presence of the spiraling-in saddle focus s_1 with the Shilnikov saddle value $\sigma = -\rho + \gamma > 0$ [with $\rho = \Re(\lambda_{1,2})$ and $\gamma = \lambda_3$, see Table VII], the behavior near this loop is complex. This is confirmed by our numerically computed streamlines. Different from the flow in an axisymmetric breakdown bubble (Sotiropoulos *et al.*, 2001), however, the present separated flow near the connection of s_1 and s_2 is intrinsically three-dimensional for $\mathrm{Re} > \mathrm{Re}_c$ and thus can support chaotic streamlines.

The region most susceptible to chaos is the main (outer) Taylor–Görtler vortex. This correlates with the three-dimensional part of the flow, which is the strongest in this region. However, the large region occupied by chaotic streamlines already at Re = 800, which is only slightly supercritical, presents a scenario quite different from cuboidal cavities, where the chaos gradually invades the regular region with increasing Re. The results show that the regular regions in the main Taylor–Görtler vortex shrink rapidly with Re. The small subvolume occupied by KAM tori in the main Taylor–Görtler vortex could be either due to a rapid monotonic destruction of large regular KAM tori, which might exist slightly above critical, or due to a global chaos existing immediately above the onset of a three-dimensional flow from which only small KAM tori can grow as Re is increased. Unfortunately, these different scenarios cannot be probed due to the long simulation times required for $\mathrm{Re} - \mathrm{Re}_c \to 0$. A similar scenario, with an abrupt onset of chaos, was found in the steady three-dimensional periodic cellular flow in

TABLE IX. Characterization of the periodic streamlines L and largest KAM tori T for $(\Gamma, \lambda) = (1, \lambda_c)$. Identification of one of the elliptic fixed points of the closed streamlines L on the Poincaré plane $x = 1/2$ for different Reynolds numbers. Additional characterizations are the minimum distance of L and T from the boundaries, Δ, and the period of a fluid element along the closed streamlines τ. Only one single arbitrary fixed point is given for each closed streamline.

Re	KAM/streamline	τ	Δ	Fixed point (y, z)
800	T_{1C}		0.3122	
	L_{1C}	6.197	0.3401	(0.483, 0.291)
	T_{1B}		0.1518	
	L_{1B}	6.260	0.1974	(0.330, 0.278)
	T_{1A}		0.0233	
	L_{1A}	13.074	0.0249	(0.131, 0.254)
	T_5		0.0179	
	L_5	40.758	0.0191	(0.119, 0.254)
	T_6		0.0098	
	L_6	25.742	0.0119	(0.103, 0.213)
850	T_{1C}		0.3031	
	L_{1C}	6.501	0.3398	(0.474, 0.268)
	T_{1B}		0.1618	
	L_{1B}	6.572	0.2013	(0.326, 0.254)
900	T_{1C}		0.3119	
	L_{1C}	6.730	0.3438	(0.656, 0.266)
	T_{1B}		0.1667	
	L_{1B}	6.805	0.2061	(0.323, 0.256)

a two-sided lid-driven cavity (Romanò *et al.*, 2017). In both systems, the two-sided cavity and the present one-sided-driven cavity, the flow structure at $\mathrm{Re} = \mathrm{Re}_c$ is characterized by several hyperbolic points or limit cycles, which can give rise to global chaos, in particular, if existing heteroclinic connections break immediately after the onset of a three-dimensional flow. On the other hand, the region of the secondary and tertiary Taylor–Görtler vortices remains regular to a large extent. This is due to the absence of hyperbolic lines in the bulk and to the fact that slightly broken connections produce a layer of chaos that remains localized near the intersection, in the Poincaré plane, of two-dimensional manifolds emerging from the critical objects at the extrema of each slightly broken heteroclinic connection.

Finally, the quantitative data given in Table IX offer benchmark data for further studies and provide necessary topological information required to characterize finite-size coherent structures in case nearly neutrally-buoyant finite-size particles are suspended in the periodic cavity flow. From the values of Δ reported in Table IX, only the flow for $\mathrm{Re} = 800$ is of interest for FSCSs since it exhibits periodic and quasiperiodic streamlines passing the moving wall closely. The flows for $\mathrm{Re} = 850$ and 900 are candidates supporting inertial coherent structures, but the minimum values of Δ are no longer small compared to the length scale of the system, a requirement for FSCSs (Romanò *et al.*, 2019).

VI. DISCUSSION AND CONCLUSION

The streamline topology in lid-driven cavities has been computed numerically for different finite-length cuboidal cavities and for Taylor–Görtler vortices in a periodic cavity with a square cross section. Due to the three-dimensional flow induced either by the finite cavity length or by a symmetry breaking instability, regions of chaotic and regular streamlines arise. Since the existence, location, character, and connection of the stationary points and limit cycles of the flow change with the Reynolds number so do the regions of regular and chaotic streamlines.

Two sources of chaotic advection are observed for finite-length and infinitely extended lid-driven cavities. In both systems, we find broken heteroclinic connections between critical points or between saddle limit cycles, which promote chaos by intersection in the Poincaré plane of their corresponding stable and unstable manifolds. The second source of chaotic advection is the resonance phenomenon, by which the resonant KAM torus breaks down, creating a pair of elliptic and hyperbolic streamlines. The newly born KAM torus about the elliptic streamline is embedded in a layer of chaos organized among the hyperbolic streamline. In the case of finite-length cavities, the three-dimensionality caused by the no-slip end walls induces a gradual growth of the chaotic subvolume. At very low Reynolds numbers, the chaotic sea develops from the solid corners and edges of the cavity and is enhanced when the heteroclinic connection between s_1 and s_2 breaks at larger Reynolds numbers. The subvolume occupied by chaotic streamlines is also increased as several resonance phenomena, i.e., breakdowns of KAM tori, arise upon a further increase of Re. A monotonic increase of the chaotic subvolume in finite-length cavities is thus observed upon an increase of Re. This scenario has been discussed in previous studies by Ishii and Adachi (2006; 2010; 2011) and Ishii *et al.* (2012). Their investigations were extended here, by using higher accuracy, quantifying the critical points, and by paying attention to the connection (transport barriers) and disconnection between the critical topological objects of the flow as a function of the Reynolds number, which affect the chaotic and regular regions of the flow.

In infinitely extended cavities, on the other hand, periodic Taylor–Görtler vortices develop as a result of symmetry breaking at a critical Reynolds number Re_c and chaos sets in at $\mathrm{Re} = \mathrm{Re}_c$ either very rapidly or even abruptly. Increasing the Reynolds number from $\mathrm{Re} = 800$ destroys the regular regions in the primary Taylor–Görtler vortex, and the saddle limit cycles W_1–W_2 and W_3–W_4 are always disconnected for $\mathrm{Re} \geq 800$. For $\mathrm{Re} \geq 850$, in particular, the broken connection between W_3 and W_4 allows for a weak exchange of fluid across the previous transport barriers, and a more extended region of chaotic streamlines is established near the axis of the Taylor–Görtler vortices. Such approximate heteroclinic connection generates, *de facto*, a region of the flow where outward transport from the secondary to the primary Taylor–Görtler vortices is remarkably reduced. Inside this region, another slightly broken heteroclinic connection between W_1 and W_2 takes place, giving rise to a slow radial advection boundary embedded in the first one. Finally, at $\mathrm{Re} = 900$, the two saddle foci s_1 and s_2 characterizing the main vortex center are found to be disconnected. Two slightly broken heteroclinic loops are, therefore, established within which two counter-rotating KAM tori are found to exist. Hence, another major difference between finite-length and infinitely extended cavities is that the chaotic subvolume is not monotonically increasing in the latter. The almost sealed volumes associated with the approximate heteroclinic loops are topologically equivalent to recirculation bubbles. Their route to chaos has well been examined by Sotiropoulos *et al.* (2001), who pointed out their structural instability with respect to flow perturbations.

The KAM tori in cavities of finite length are all found to pass very close to the moving lid. This property of the flow is favoring Lagrangian finite-size coherent structures of particles in dilute suspensions via the mechanism described by Hofmann and Kuhlmann (2011) and Romanò *et al.* (2019). Accordingly, particles can be displaced from the chaotic sea to regular regions of the flow near the moving lid. In order for this mechanism to be effective, the particle size would have to be small and of the same order of magnitude as the distance of the KAM structures from the moving wall. For this reason, the distances Δ of the closed streamlines and of the largest reconstructible KAM tori have been reported in Tables III–V. For periodic Taylor–Görtler vortices, on the other hand, the KAM tori are located relatively far from the bounding cavity walls, except possibly for very slightly supercritical driving. Therefore, Lagrangian coherent particle structures are not expected to arise in steady periodic lid-driven Taylor–Görtler vortices (see Table IX).

Regular regions near the center of finite-length cavities are found for $\Lambda = 2$ (see $\mathrm{Re} = 400$, T_{1M}) and were also found by Ishii and Adachi (2006) for $\Lambda = 6.55$ and $\mathrm{Re} = 500 < \mathrm{Re}_c\,(\Lambda \to \infty)$. These regular regions are due to the change of sign of the spanwise velocity component w and to the progressive takeover of the two-dimensional flow in the midplane for $\Lambda \to \infty$ and $\mathrm{Re} < \mathrm{Re}_c$. It is interesting to note that Ishii and Adachi (2006) also found KAM tori near the symmetry plane for $\Lambda = 6.55$ and $\mathrm{Re} = 850$. For the

same parameters, Albensoeder *et al.* (2001b) experimentally found Taylor–Görtler vortices only near the symmetry plane. Therefore, it would be interesting to investigate the implications for the flow topology of the competition between weak Taylor–Görtler vortices due to a bulk flow instability and a weak end-wall-driven flow in finite-length cavities. However, even for a subcritical flow with $\mathrm{Re} \leq \mathrm{Re}_c$, e.g., for $\mathrm{Re} = 400$, the creation/annihilation of KAM tori upon a quasi-continuous variation of the aspect ratio Λ is another open question. We also note that stagnation points can arise in the bulk and contribute to chaotic advection (Contreras *et al.*, 2017; Romanò *et al.*, 2017). But such stagnation points have not been found in the present study.

A further perspective of this study concerns finite-size coherent particle structures in one-sided lid-driven cavities. This type of particle accumulation phenomenon, already reported in a recent study (Kuhlmann *et al.*, 2016; Wu *et al.*, 2017a; 2017b), deserves further investigation in order to relate the particle motion to the Lagrangian flow topology considered herein.

The improvement of computational resources has recently made possible a numerically accurate characterization of the Lagrangian topology for spatially three-dimensional flows. We, therefore, expect that succeeding studies of three-dimensional cavity flows will shed further light on the evolution of streamline chaos in three-dimensional incompressible flows and to the role of symmetry-breaking instabilities.

DATA AVAILABILITY

The data that support the findings of this study are available from the corresponding author upon reasonable request.

REFERENCES

Albensoeder, S. and Kuhlmann, H. C., "Linear stability of rectangular cavity flows driven by anti-parallel motion of two facing walls," J. Fluid Mech. **458**, 153–180 (2002).

Albensoeder, S. and Kuhlmann, H. C., "Stability balloon for the double-lid-driven cavity flow," Phys. Fluids **15**, 2453–2456 (2003).

Albensoeder, S. and Kuhlmann, H. C., "Accurate three-dimensional lid-driven cavity flow," J. Comput. Phys. **206**, 536–558 (2005).

Albensoeder, S. and Kuhlmann, H. C., "Nonlinear three-dimensional flow in the lid-driven square cavity," J. Fluid Mech. **569**, 465–480 (2006).

Albensoeder, S., Kuhlmann, H. C., and Rath, H. J., "Multiplicity of steady two-dimensional flows in two-sided lid-driven cavities," Theor. Comp. Fluid Dyn. **14**, 223–241 (2001a).

Albensoeder, S., Kuhlmann, H. C., and Rath, H. J., "Three-dimensional centrifugal-flow instabilities in the lid-driven cavity problem," Phys. Fluids **13**, 121–135 (2001b).

Alleborn, N., Raszillier, H., and Durst, F., "Lid-driven cavity with heat and mass transport," Int. J. Heat Mass Transf. **42**, 833–853 (1999).

Anderson, P. D., Galaktionov, O. S., Peters, G. W. M., van de Vosse, F. N., and Meijer, H. E. H., "Chaotic fluid mixing in non-quasi-static time-periodic cavity flows," Int. J. Heat Fluid Flow **21**, 176–185 (2000).

Anderson, P. D., Galaktionov, O. S., Peters, G. W. M., Vosse, F. N. V. D., and Meijer, H. E. H., "Analysis of mixing in three-dimensional time-periodic cavity flows," J. Fluid Mech. **386**, 149–166 (1999).

Arbabi, H. and Mezić, I., "Prandtl-Batchelor theorem for flows with quasiperiodic time dependence," J. Fluid Mech. **862**, R1 (2019).

Aref, H., "Integrable, chaotic and turbulent vortex motion in two-dimensional flows," Annu. Rev. Fluid Mech. **15**, 345–389 (1983).

Aref, H., "Stirring by chaotic advection," J. Fluid Mech. **143**, 1–21 (1984).

Aref, H., "The numerical experiment in fluid mechanics," J. Fluid Mech. **173**, 15–41 (1986).

Aref, H., "Chaotic advection of fluid particles," Phil. Trans. R. Soc. Lond. A: Phys. Eng. Sci. **333**, 273–288 (1990).

Aref, H., "The development of chaotic advection," Phys. Fluids **14**, 1315–1325 (2002).

Aref, H. and Balachandar, S., "Chaotic advection in a Stokes flow," Phys. Fluids **29**, 3515–3521 (1986).

Aref, H., Blake, J. R., Budišić, M., Cardoso, S. S., Cartwright, J. H. E., Clercx, H. J. H., Omari, K. E., Feudel, U., Golestanian, R., Gouillart, E., van Heijst, G. F., Krasnopolskaya, T. S., Guer, Y. L., MacKay, R. S., Meleshko, V. V., Metcalfe, G., Mezić, I., de Moura, A. P. S., Piro, O., Speetjens, M. F. M., Sturman, R., Thiffeault, J.-L., and Tuval, I., "Frontiers of chaotic advection," Rev. Mod. Phys. **89**, 025007 (2017).

Arnol'd, V. I., *Mathematical Methods of Classical Mechanics* (Springer, 1978).

Arter, W., "Ergodic stream-lines in steady convection," Phys. Lett. **97A**, 171–174 (1983).

Auteri, F., Parolini, N., and Quartapelle, L., "Numerical investigation on the stability of singular driven cavity flow," J. Comput. Phys. **183**, 1–25 (2002).

Bajer, K., "Hamiltonian formulation of the equations of streamlines in three-dimensional steady flow," Chaos Solitons Fractals **4**, 895–911 (1994).

Barmak, I., Romanò, F., and Kuhlmann, H. C., "Particle accumulation in high-Prandtl-number liquid bridges," Proc. Appl. Math. Mech. **19**, e201900058 (2019).

Batchelor, G. K., "On steady laminar flow with closed streamlines at large Reynolds numbers," J. Fluid Mech. **1**, 177–190 (1956).

Biemond, J. J. B., de Moura, A. P. S., Károlyi, G., Grebogi, C., and Nijmeijer, H., "Onset of chaotic advection in open flows," Phys. Rev. E **78**, 016317 (2008).

Bödewadt, U. T., "Die Drehströmung über festem Grunde," Z. Angew. Math. Mech. **20**, 241–253 (1940).

Botella, O. and Peyret, R., "Benchmark spectral results on the lid-driven cavity flow," Comp. Fluids **27**, 421–433 (1998).

Broer, H. W., Huitema, G. B., and Sevryuk, M. B., *Mathematical Methods of Classical Mechanics* (Springer, 2009).

Brøns, M., Voigt, L. K., and Sœrensen, J. N., "Topology of vortex breakdown bubbles in a cylinder with a rotating bottom and a free surface," J. Fluid Mech. **428**, 133–148 (2001).

Broomhead, D. S. and Ryrie, S. C., "Particle paths in wavy vortices," Nonlinearity **1**, 409–434 (1988).

Bruneau, C.-H. and Saad, M., "The 2d lid-driven cavity problem revisited," Comp. Fluids **35**, 326–348 (2006).

Burggraf, O. R., "Analytical and numerical studies of the structure of steady separated flows," J. Fluid Mech. **24**, 113–151 (1966).

Cartwright, J. H. E., Feingold, M., and Piro, O., "Chaotic advection in three-dimensional unsteady incompressible laminar flow," J. Fluid Mech. **316**, 259–284 (1996).

Cheng, C.-Q. and Sun, Y.-S., "Existence of invariant tori in three-dimensional measure-preserving mappings," Celest. Mech. Dyn. Astron. **47**, 275–292 (1989a).

Cheng, C.-Q. and Sun, Y.-S., "Existence of periodically invariant curves in 3-dimensional measure-preserving mappings," Celest. Mech. Dyn. Astron. **47**, 293–303 (1989b).

Cheng, C. Q. and Sun, Y. S., "Existence of invariant tori in three-dimensional measure-preserving mappings," Celest. Mech. Dyn. Astron. **47**, 275–292 (1990).

Chernikov, A. A. and Schmidt, G., "Chaotic streamlines in convective cells," Phys. Lett. A **169**, 51–56 (1992).

Chiang, T. P. and Sheu, W. H., "Numerical prediction of eddy structure in a shear-driven cavity," Comp. Mech. **20**, 379–396 (1997).

Chien, W.-L., Rising, H., and Ottino, J. M., "Laminar mixing and chaotic mixing in several cavity flows," J. Fluid Mech. **170**, 355–377 (1986).

Contreras, P. S., Ataei-Dadavi, I., Speetjens, M. F. M., Kleijn, C. R., Tummers, M. J., and Clercx, H. J. H., "Topological equivalence between two classes of three-dimensional steady cavity flows: A numerical-experimental analysis," Phys. Fluids **31**, 123601 (2019).

Contreras, P. S., Speetjens, M. F. M., and Clercx, H. J. H., "Lagrangian transport in a class of three-dimensional buoyancy-driven flows," J. Fluid Mech. **832**, 5–40 (2017).

Crighton, D. G., "Airframe noise," in *Aeroacoustics of Flight Vehicles: Theory and Practice. Volume 1: Noise Sources*, edited by H. H. Hubbard (NASA Office of Management, Scientific and Technical Information Program, 1991), pp. 391–447.

Davey, A., "The growth of Taylor vortices in flow between rotating cylinders," J. Fluid Mech. **14**, 336–368 (1962).

Davis, A. M. J. and Smith, S. G. L., "Three-dimensional corner eddies in Stokes flow," Fluid Dyn. Res. **46**, 015509 (2014).

Dormand, J. R. and Prince, P. J., "A family of embedded Runge-Kutta formulae," J. Comput. Appl. Math. **6**, 19–26 (1980).

Escudier, M. P., "Observations of the flow produced in a cylindrical container by a rotating endwall," Exp. Fluids **2**, 189–196 (1984).

Fischer, P. F., Lottes, J. W., and Kerkemeier, S. G., see https://nek5000.mcs.anl.gov/ for "NEK5000 Web Page" (2008).

Fountain, G. O., Khakhar, D. V., Mezić, I., and Ottino, J. M., "Chaotic mixing in a bounded three-dimensional flow," J. Fluid Mech. **417**, 265–301 (2000).

Franjione, J. G., Leong, C.-W., and Ottino, J. M., "Symmetries within chaos: A route to effective mixing," Phys. Fluids A **1**, 1772–1783 (1989).

Gaskell, P. H., Summers, J. L., Thompson, H. M., and Savage, M. D., "Creeping flow analyses of free surface cavity flows," Theor. Comput. Fluid Dyn. **8**, 415–433 (1996).

Ghia, U., Ghia, K. N., and Shin, C. T., "High-Re solutions for incompressible flow using the Navier-Stokes equations and a multigrid method," J. Comput. Phys. **48**, 387–411 (1982).

Gomilko, A. M., Malyuga, V. S., and Meleshko, V. V., "On steady Stokes flow in a trihedral rectangular corner," J. Fluid Mech. **476**, 159–177 (2003).

Haller, G., "Lagrangian coherent structures," Annu. Rev. Fluid Mech. **47**, 137–162 (2015).

Hofmann, E. and Kuhlmann, H. C., "Particle accumulation on periodic orbits by repeated free surface collisions," Phys. Fluids **23**, 0721106 (2011).

Hwang, W. R., Anderson, P. D., and Hulsen, M. A., "Chaotic advection in a cavity flow with rigid particles," Phys. Fluids **17**, 043602 (2005).

Ishii, K. and Adachi, S., "Numerical analysis of 3D vortical cavity flow," Proc. Appl. Math. Mech. **6**, 871–874 (2006).

Ishii, K. and Adachi, S., "Transition of streamline patterns in three-dimensional cavity flows," Theor. Appl. Mech. Jpn. **59**, 203–210 (2010).

Ishii, K. and Adachi, S., "Dependence on the aspect ratio of streamline patterns in three-dimensional cavity flows," Theor. Appl. Mech. Jpn. **60**, 51–61 (2011).

Ishii, K. and Iwatsu, R., "Numerical simulation of the Lagrangian flow structure in a driven cavity," in *Topological Fluid Mechanics*, edited by H. K. Moffat and A. Tsinober (Cambridge University Press, 1989), pp. 54–63.

Ishii, K., Ota, C., and Adachi, S., "Streamlines near a closed curve and chaotic streamlines in steady cavity flows," Proc. IUTAM **5**, 173–186 (2012).

Jacono, D. L., Nazarinia, M., and Brøns, M., "Experimental vortex breakdown topology in a cylinder with a free surface," Phys. Fluids **21**, 111704-1–111704-4 (2009).

Karniadakis, G. E., Israeli, M., and Orszag, S. A., "High-order splitting methods for the incompressible Navier–Stokes equations," J. Comput. Phys. **97**, 414–443 (1991).

Koseff, J. R. and Street, R. L., "The lid-driven cavity flow: A synthesis of qualitative and quantitative observations," J. Fluids Eng. **106**(4), 390–398 (1984).

Kroujiline, D. and Stone, H. A., "Chaotic streamlines in steady bounded three-dimensional Stokes flows," Physica D **130**, 105–132 (1999).

Kuhlmann, H. C. and Romanò, F., "The lid-driven cavity," in *Computational Modelling of Bifurcations and Instabilities in Fluid Dynamics*, Computational Methods in Applied Sciences Vol. 50, edited by A. Gelfgat (Springer, 2019), pp. 233–309.

Kuhlmann, H. C., Romanò, F., Wu, H., and Albensoeder, S., "Particle-motion attractors due to particle-boundary interaction in incompressible steady three-dimensional flows," in *The 20th Australasian Fluid Mechanics Conference*, edited by G. Ivey, T. Zhou, N. Jones, and S. Draper (Australasian Fluid Mechanics Society, 2016), 102 pp., Paper No. 449.

Leong, C. W. and Ottino, J. M., "Experiments on mixing due to chaotic advection in a cavity," J. Fluid Mech. **209**, 463–499 (1989).

Leriche, E. and Labrosse, G., "Are there localized eddies in the trihedral corners of the Stokes eigenmodes in cubical cavity?," Comp. Fluids **43**, 98–101 (2011).

Mezić, I. and Wiggins, S., "On the integrability and perturbation of three-dimensional fluid flows with symmetry," J. Nonlinear Sci. **4**, 157–194 (1994).

Moffatt, H. K., "Viscous and resistive eddies near a sharp corner," J. Fluid Mech. **18**, 1–18 (1964).

Mukin, R. V. and Kuhlmann, H. C., "Topology of hydrothermal waves in liquid bridges and dissipative structures of transported particles," Phys. Rev. E **88**, 053016 (2013).

Muldoon, F. H. and Kuhlmann, H. C., "Coherent particulate structures by boundary interaction of small particles in confined periodic flows," Physica D **253**, 40–65 (2013).

Oteski, L., Duguet, Y., and Pastur, L. R., "Lagrangian chaos in confined two-dimensional oscillatory convection," J. Fluid Mech. **759**, 489–519 (2014).

Ottino, J. M., *The Kinematics of Mixing: Stretching, Chaos, and Transport* (Cambridge University Press, Cambridge, 1989).

Ottino, J. M., Leong, C. W., Rising, H., and Swanson, P. D., "Morphological structures produced by mixing in chaotic flows," Nature **333**, 419–425 (1988).

Pai, S. A., Prakash, P., and Patnaik, B. S. V., "Numerical simulation of chaotic mixing in lid driven cavity: Effect of passive plug," Eng. Appl. Comput. Fluid Mech. **7**, 406–418 (2013).

Pouransari, Z., Speetjens, M. F. M., and Clercx, H. J. H., "Formation of coherent structures by fluid inertia in three-dimensional laminar flows," J. Fluid Mech. **654**, 5–34 (2010).

Povitsky, A., "Three-dimensional flow with elevated helicity in driven cavity by parallel walls moving in perpendicular directions," Phys. Fluids **29**, 083601 (2017).

Prandtl, L., "Über Flüssigkeitsbewegung bei sehr kleiner Reibung," in *Verhdlg. III Intern. Math.-Kongr.* (Teubner, Leipzig, 1904), pp. 484–491.

Ramanan, N. and Homsy, G. M., "Linear stability of lid-driven cavity flow," Phys. Fluids **6**, 2690–2701 (1994).

Romanò, F., Albensoeder, S., and Kuhlmann, H. C., "Topology of three-dimensional steady cellular flow in a two-sided anti-parallel lid-driven cavity," J. Fluid Mech. **826**, 302–334 (2017).

Romanò, F., Hajisharifi, A., and Kuhlmann, H. C., "Cellular flow in a partially fillled rotating drum: Regular and chaotic advection," J. Fluid Mech. **825**, 631–650 (2017).

Romanò, F. and Kuhlmann, H. C., "Numerical investigation of the interaction of a finite-size particle with a tangentially moving boundary," Int. J. Heat Fluid Flow **62**, 75–82 (2016).

Romanò, F. and Kuhlmann, H. C., "Particle–boundary interaction in a shear-driven cavity flow," Theor. Comput. Fluid Dyn. **31**, 427–445 (2017a).

Romanò, F. and Kuhlmann, H. C., "Smoothed-profile method for momentum and heat transfer in particulate flows," Int. J. Num. Meth. Fluids **83**, 485–512 (2017b).

Romanò, F. and Kuhlmann, H. C., "Finite-size Lagrangian coherent structures in thermocapillary liquid bridges," Phys. Rev. Fluids **3**, 094302 (2018).

Romanò, F. and Kuhlmann, H. C., "Finite-size coherent structures in thermocapillary liquid bridges," Int. J. Microgravity Sci. Appl. **36**, 360201 (2019).

Romanò, F., Kunchi Kannan, P., and Kuhlmann, H. C., "Finite-size Lagrangian coherent structures in a two-sided lid-driven cavity," Phys. Rev. Fluids **4**, 024302 (2019).

Romanò, F., Wu, H., and Kuhlmann, H. C., "A generic mechanism for finite-size coherent particle structures," Int. J. Multiphase Flow **111**, 42–52 (2019).

Schuster, H. G., *Deterministic Chaos: An Introduction* (Wiley-VCH, Weinheim, 2005).

Scott, J. F., "Moffatt-type flows in a trihedral cone," J. Fluid Mech. **725**, 446–461 (2013).

Shankar, P. N., "Three-dimensional stokes flow in a cylindrical container," Phys. Fluids **10**, 540–549 (1998).

Shankar, P. N. and Deshpande, M. D., "Fluid mechanics in the driven cavity," Ann. Rev. Fluid Mech. **32**, 93–136 (2000).
Sheu, T. W. H. and Tsai, S. F., "Flow topology in a steady three-dimensional lid-driven cavity," Comp. Fluids **31**, 911–934 (2002).
Sotiropoulos, F., Ventikos, Y., and Lackey, T. C., "Chaotic advection in three-dimensional stationary vortex-breakdown bubbles: Šil'nikov's chaos and the devil's staircase," J. Fluid Mech. **444**, 257–297 (2001).
Spohn, A., Mory, M., and Hopfinger, E. J., "Observations of vortex breakdown in an open cylindrical container with a rotating bottom," Exp. Fluids **14**, 70–77 (1993).
Taylor, G. I., "Similarity solutions of hydrodynamic problems," in *Aeronautics and Astronautics (Durand Anniversary Volume)* (Pergamon, 1960), pp. 21–28.
Taylor, G. I., "On scraping viscous fluid from a plane surface," in *The Scientific Papers of Sir Geoffrey Ingram Taylor*, Vol. IV: Mechanics of Fluids—Miscellaneous Papers, edited by G. K. Batchelor (Cambridge University Press, Cambridge, UK, 1962), pp. 410–413.
Tél, T. and Gruiz, M., *Chaotic Dynamics* (Cambridge University Press, 2006).
Tsorng, S. J., Capart, H., Lai, J. S., and Young, D. L., "Three-dimensional tracking of the long time trajectories of suspended particles in a lid-driven cavity flow," Exp. Fluids **40**, 314–328 (2006).
Tsorng, S. J., Capart, H., Lo, D. C., Lai, J. S., and Young, D. L., "Behaviour of macroscopic rigid spheres in lid-driven cavity flow," Int. J. Multiphase Flow **34**, 76–101 (2008).
Wang, C. Y., "Stagnation flow on the surface of a quiescent fluid—An exact solution of the Navier–Stokes equations," Q. Appl. Math. **43**, 215–223 (1985).
Wang, C. Y., "Impinging stagnation flows," Phys. Fluids **30**, 915–917 (1987).
Wiggins, S., "Coherent structures and chaotic advection in three dimensions," J. Fluid Mech. **654**, 1–4 (2010).
Wu, H., Romanò, F., and Kuhlmann, H. C., "Attractors for the motion of finite-size particles in a lid-driven cavity," in *Fachtagung Experimentelle Strömungsmechanik* (German Association for Laser Anemometry GALA e.V., Karlsruhe, Germany, 2017a), ISBN: 978-3-9816764-3-3.
Wu, H., Romanò, F., and Kuhlmann, H. C., "Attractors for the motion of finite-size particles in a two-sided lid-driven cavity," Proc. Appl. Math. Mech. **17**, 669–670 (2017b).
Xu, B. and Gilchrist, J. F., "Shear migration and chaotic mixing of particle suspensions in a time-periodic lid-driven cavity," Phys. Fluids **22**, 053301 (2010).
Young, D. L., Jane, S. C., Lin, C. Y., Chiu, C. L., and Chen, K. C., "Solutions of 2D and 3D Stokes laws using multiquadrics method," Eng. Anal. Bound. Elem. **28**, 1233–1243 (2004).
Znaien, J., Speetjens, M. F. M., Trieling, R. R., and Clercx, H. J. H., "Observability of periodic lines in three-dimensional lid-driven cylindrical cavity flows," Phys. Rev. E **85**, 066320-1–066320-14 (2012).